Title: Odor and reward-evoked GABAergic neuronal activity in the basal forebrain influences olfactory-guided behavior in mice

Abbreviated title: Basal forebrain GABA impacts olfactory behavior

Authors: Elizabeth H. Moss[1,3*], Evelyne K. Tantry[1], Elaine Le[1], Katie L. Brandel-Ankrapp[2], Benjamin R. Arenkiel[1]

Affiliations: [1]Department of Molecular and Human Genetics, Baylor College of Medicine, Houston TX, 97030, USA; [2]Neuroscience Graduate Program, Baylor College of Medicine, Houston, TX, 97030, USA, [3]Present Address: Department of Anesthesiology and Perioperative Medicine, Oregon Health & Science University, Portland, OR, 97239, USA

*Correspondence to mosse@ohsu.edu

Key words: Olfaction, Basal Forebrain, Parvalbumin, Somatostatin, go/no-go, decision-making

Pages: 49

Figures: 5

Tables: 3

Word Count: Abstract: 187, Introduction: 650 words, Discussion: 1379

Conflict of Interest Statement: The authors declare no competing financial interests.

Acknowledgements: This work was supported by the NIH through NINDS and the BRAIN Initiative (U01NS111692 and R01NS078294 to BRA) and NIDCD and the BRAIN Initiative (K99DC019505 to EHM).

ABSTRACT

Sensory perception relies on the flexible detection and interpretation of stimuli across variable contexts, conditions, and behavioral states. The basal forebrain is a hub for behavioral state regulation, supplying dense cholinergic and GABAergic projections to various brain regions involved in sensory processing. Of GABAergic neurons in the basal forebrain, parvalbumin (PV) and somatostatin (SST) subtypes serve opposing roles towards regulating behavioral states. To elucidate the role of basal forebrain circuits in sensory-guided behavior, we investigated GABAergic signaling dynamics during odor-guided decision-making. We used fiber photometry to record cell type-specific basal forebrain activity during an odor discrimination task and correlated temporal patterns of PV and SST neuronal activity with olfactory task performance. We found that while both PV-expressing and SST-expressing GABAergic neurons were activated by odors, PV neurons were selectively suppressed by reward whereas SST neurons were activated. Notably, chemogenetic inhibition of BF SST neurons modestly altered decision bias to favor reward-seeking while optogenetic inhibition of BF PV neurons during odor presentations improved discrimination accuracy. Together, these results suggest that the bidirectional activity of GABAergic basal forebrain neuron subtypes distinctly influence perception and decision-making during olfactory guided behavior.

SIGNIFICANCE STATEMENT

This study reveals distinct roles for basal forebrain GABAergic neurons in odor perception and odor-guided decision-making. Fiber photometry shows that basal forebrain parvalbumin-expressing neurons are selectively suppressed by rewards, while somatostatin-expressing neurons are activated, establishing the unique recruitment of these GABAergic neurons during behavioral reinforcement. Chemogenetic and optogenetic interventions demonstrate divergent roles for these neuronal subtypes in reward-seeking behavior and odor perception. This research provides new insights into how GABAergic neurons in the basal forebrain shape sensory perception and decision-making.

INTRODUCTION

Behavioral states potently influence neural circuit function and control information processing from the level of sensory perception to cognition, learning, and memory. The basal forebrain (BF) is involved in behavioral state regulation, with BF circuits controlling directed attention (Sarter and Bruno, 1999; Sarter et al., 2001; Hasselmo and McGaughy, 2004; Herrero et al., 2008), sensory processing (Parikh et al., 2007; Chaudhury et al., 2009; Pinto et al., 2013; Bendahmane et al., 2016; Gritton et al., 2016; Ogg et al., 2018), feeding behavior (Herman et al., 2016; Patel et al., 2019), reward prediction and salience (Lau and Salzman, 2008; Lin and Nicolelis, 2008; Hangya et al., 2015; Ledbetter et al., 2016; Zhang et al., 2019), learning and memory (Muir et al., 1993; Devore et al., 2015; Harrison et al., 2016; Zheng et al., 2018), and arousal (Semba, 1991; Szymusiak, 1995; Sarter and Bruno, 1999; Szymusiak et al., 2000; Lau and Salzman, 2008; Anaclet et al., 2015; Xu et al., 2015). BF projections robustly target both sensory and cognitive circuits and their degeneration is thought to underlie cognitive deficits in disease (Bigl et al., 1982; Grothe et al., 2010; Ballinger et al., 2016; Chaves-Coira et al., 2016; Gielow and Zaborszky, 2017). During learning, BF responses to sensory stimuli are modulated by reward expectation (Lin and Nicolelis, 2008; Hangya et al., 2015; Zhang et al., 2019), supporting that BF circuits integrate sensory input with internal information about reward expectation. Additionally, inhibition of the BF impairs attention in response to motivationally salient stimuli (Tashakori-Sabzevar and Ward, 2018). Intriguingly, both cholinergic and non-cholinergic BF neurons show distinct activity in response to sensory stimuli, and play different roles in reward-based learning (Hangya et al., 2015; Patel et al., 2019; Böhm et al., 2020; Nunez-Parra et al., 2020; Hanson et al., 2021). Thus, to better understand how BF circuits mediate state-dependent effects on sensory perception and related behaviors, it is necessary to determine the dynamic activity patterns of specific cell types in the BF and how they are modulated across different behavioral contexts.

The mouse olfactory system is an ideal model for examining the influence of BF modulation on sensory perception and decision-making behavior because both the olfactory bulb and olfactory cortex receive significant cholinergic and GABAergic input from the BF (Woolf et al., 1986; Zaborszky et al.,

80 1986; Nunez-Parra et al., 2013; Sanz Diez et al., 2019; Böhm et al., 2020). Olfactory behaviors,
81 including odor discrimination and odor-guided decision-making can be measured via convenient
82 behavioral assays. Studies that have examined the impact of BF neurons on odor processing have
83 found that inhibiting BF GABAergic neurons impairs fine odor discrimination in a cross-habituation test
84 (Nunez-Parra et al., 2013), and ablating BF cholinergic neurons impairs discrimination in a go/no-go
85 task (Zheng et al., 2022). Moreover, both cholinergic and GABAergic BF neurons respond to odors and
86 reinforcement in go/no-go discrimination tasks (Hangya et al., 2015; Nunez-Parra et al., 2020). We
87 have previously shown that BF GABAergic neuronal activity peaks during odor presentations and is
88 suppressed by reward delivery in a go/no-go task – dynamics which mirror changes in BF cholinergic
89 tone (Hanson et al., 2021). This demonstrates that BF GABAergic neurons are acutely and
90 bidirectionally regulated during odor discrimination tasks with positive reinforcement. These
91 experiments, however, did not differentiate subtypes of GABAergic neurons. Towards understanding
92 how specific BF cell types respond to sensory stimulation, decision-making, and discrimination learning,
93 we used fiber photometry to record BF PV and SST neuronal activity while mice performed an
94 olfactory-cued go/no-go discrimination task. Our data reveal distinct patterns of neuronal activity in PV
95 and SST BF neurons that are uniquely correlated with different aspects of task performance. Further,
96 chemogenetic inhibition of BF SST neurons modestly increased decision bias in favor of reward-
97 seeking, while optogenetic inhibition of BF PV neurons during odor presentations improved odor
98 discrimination. Together these findings highlight the unique contributions of BF PV and SST neurons to
99 odor-guided task performance and decision making.

100

101 **RESULTS**

102 ***BF PV neurons are excited by odor and suppressed by reward delivery***

103 To assess PV neuronal responses during odor discrimination learning, we selectively expressed the
104 genetically encoded calcium indicator GCaMP8s in BF PV neurons by injecting an AAV expressing
105 Cre-dependent GCaMP8s (AAV hsyn-FLEX-GCaMP8s) into the BF of PV-Cre mice. At the same time,

we placed a fiberoptic implant over the horizontal limb of the diagonal band of Broca (HDB) in the BF (**Figure 1A**). Implant and viral targeting were verified via post hoc immunofluorescence imaging (**Figure 1B, C**). Implanted mice were then trained and tested on a go/no-go paradigm as previously described (Hanson et al., 2021). During training, mice learned to distinguish an S+ odorant associated with a water reward from an S- odorant not associated with reward. In this odor-cued go/no-go discrimination task, there were four trial outcomes depending on the odor presented and the decision to go or not go for a reward. Retrieving the water reward upon S+ cue presentation was considered a "Hit". Not retrieving water after S+ presentation was considered a "Miss". Attempting to retrieve water upon S- cue presentation was a "False Alarm". Finally, initiating a new trial after S- presentation was considered a "Correct Reject" (**Figure 1D**). Punishment for False Alarm trials consisted of a 4 second time-out period in which they were unable to initiate another trial. Mice were trained on the go/no-go task for 10-14 days prior to testing and fiber photometry recording. After training, mice were tested on novel odor pairings (**Table 1** in methods) while neuronal activity was recorded with fiber photometry. To quantify behavioral performance and decision making we used the signal detection theory measures of d' and criterion (C). d' measures the sensitivity of odor discrimination with higher d' values indicating more accurate discrimination between the S+ and S- odors and chance equaling zero. Criterion measures the bias in decision-making toward reward seeking (go) or non-reward-seeking (no-go) behavior with negative C values indicating a bias towards reward-seeking behavior. Notably, in our go/no-go task, S+ and S- odors are presented with equal frequency so that optimal decision bias in the task is 0. However, mice performed this task with a significantly negative decision bias (i.e., a bias towards reward-seeking, C: -0.11 ± 0.05, $p < 0.05$ one sample t test) likely because the positive possibility of a water reward outweighed the negative possibility of a timeout punishment. Notably, all mice effectively learned to discriminate new pairs of S+ and S- odors with performance significantly above chance within 400 trials (d': 2.30 ± 0.17, $p < 0.0001$, $t = 14.56$, $df = 26$, one-sample t test).

To determine HDB PV neuronal activity across phases of the go/no-go task and different trial outcomes, photometry traces were first aligned to odor port entry times and sorted by trial type. We

observed a distinct pattern of PV neuronal activity over the course of a go/no-go trial, with excitation during odor presentations across all trial types, and suppression following reward delivery in Hit trials (**Figure 1E**). The peak in z-scored PV neuronal activity during odor presentation was equivalent across all four trial types (**Figure 1F**, Hit: 1.73 ± 0.21, Miss: 1.71 ± 0.20, Correct Reject: 1.64 ± 0.20, False Alarm: 1.68 ± 0.21 z score, $p = 0.40$, $F = 0.93$, $df = 23$, RM one-way ANOVA) suggesting that the response was not odor specific (S+ vs. S-), predictive of behavioral choice (go vs. no-go), or predictive of accuracy (correct vs incorrect decisions) on individual trials. To further examine the response of PV neurons to reward seeking and reinforcement, we realigned Hit and False Alarm trials to the timing of reward port entry (**Figure 1G**). Quantifying the area under the curve (AUC) for the first 5 seconds after reward port entry showed that PV neuronal activity was strongly suppressed in Hit, but not False Alarm trials (**Figure 1H**, Hit: -2.52 ± 0.50, False Alarm: 2.60 ± 0.40 z score*s, $p < 0.001$, $t = 6.88$, $df = 5$, paired t test), implying that the suppression was a consequence of obtaining the water reward. Notably, this pattern of odor-evoked excitation and reward-evoked suppression mirrored the changes in both the cholinergic tone and general GABAergic neuronal activity we have previously described in the HDB (Hanson et al., 2021). These data indicate that PV neurons in the HDB respond bidirectionally to the odor cue and positive reinforcement during go/no-go task performance, thus raising the question of whether PV neuronal activity controls, or is modulated by, task performance across sessions and/or learning within sessions.

To determine the extent to which PV neuronal activity was related to task performance, we examined correlations between the odor response magnitude, reward response magnitude, behavioral performance, and decision making. Using linear regression and Pearson's correlation to examine the relationship between PV neuronal activity and sensitivity across sessions, we found that d' was negatively correlated with odor response magnitude in all trial types (**Figure 1I**, Hit slope = -0.41 ± 0.17, $r = -0.44$, $p < 0.05$; Miss slope = -0.42 ± 0.14, $r = -0.52$, $p < 0.01$; Correct Reject slope = -0.44 ± 0.17, $r = -0.45$, $p < 0.05$; False Alarm slope = -0.43 ± 0.17, $r = -0.45$, $p < 0.05$). The slopes and intercepts between trial types were not significantly different (slopes: $p = .99$, $F = 0.005$, $df = 100$, pooled slope = -

158 0.43; intercepts: $p = 0.92$, $F = 0.16$, $df = 103$, pooled intercept = 2.83). These data show that in
159 sessions where the average odor response among HDB PV neurons was higher, overall performance
160 on the discrimination task was worse. Using the same analysis to compare decision bias to PV
161 neuronal activity, we found that C was not correlated with the magnitude of the odor-evoked peak for
162 any trial type (Hit slope = -0.76 $\pm$ 0.5, $r = -0.29$, $p = 0.15$; Miss slope = -0.81 $\pm$ 0.4, $r = -0.36$, $p = 0.07$;
163 Correct Reject slope = -0.76 $\pm$ 0.5, $r = -0.28$, $p = 0.15$; False Alarm slope = -0.62 $\pm$ 0.5, $r = -0.23$, $p =$
164 0.25). The slopes and intercepts were also not different between trial types (slopes: $p = .99$, $F = 0.03$, df
165 = 100, pooled slope = -0.74; intercepts: $p = 0.94$, $F = 0.12$, $df = 103$, pooled intercept = 1.87). Together
166 these data help distinguish between neuronal activity patterns related to decision making behavior and
167 task difficulty (i.e. the discriminability of individual odor pairs). While these data do not indicate whether
168 the magnitude of the PV odor response influences odor discrimination, they do suggest that the
169 observed odor-evoked peak in HDB PV neuronal activity is related to odor discriminability, but not
170 decision-making behavior in this go/no-go task.

171 Next, we examined whether PV neuronal activity in response to reward delivery was related to
172 odor discriminability or decision-making behavior. Using the same linear regression and Pearson's
173 correlation analyses, we found no correlation between d' and the magnitude of the reward-evoked
174 suppression in Hit or False Alarm trials (**Figure 1J,** Hit slope = -0.37 $\pm$ 0.48, $r = -0.15$, $p = 0.45$; False
175 Alarm slope = -0.131 $\pm$ 0.52, $r = -0.05$, $p = 0.80$). However, we noted a significant difference between
176 the intercepts of the regressions for Hit and False Alarm trials (Hit intercept = -1.68 $\pm$ 1.06, False Alarm
177 intercept = 2.90 $\pm$ 1.13; $p < 0.0001$, $F = 100.4$, $df = 51$), confirming that the difference in AUC between
178 Hit and False Alarm trials is consistent across sessions with a range of d'. At the same time, we found a
179 significant negative correlation between C and the magnitude of reward evoked suppression in Hit trials
180 (**Figure 1K,** slope = -4.08 $\pm$ 1.10, $r = -0.59$, $p < 0.01$). This correlation was absent in unrewarded False
181 Alarm trials (slope = -0.84 $\pm$ 1.44, $r = -0.12$ $p = 0.57$), suggesting that the suppression of PV neuronal
182 activity after reward delivery is related to decision making-behavior. However, these data do not reveal
183 whether the greater suppression of BF PV neurons drives more optimal decision-making behavior or

184 vice versa. Intercepts were also significantly different between Hit and False Alarm trials (Hit intercept =
185 -2.88 ± 1.10, False Alarm intercept = 2.54 ± 1.44; $p < 0.0001$, $F = 113$, $df = 51$), confirming that the
186 reward-evoked suppression of PV neuronal activity was present across sessions with a range of
187 decision biases.

188 Correlations between session averages of d' and criterion do not help determine whether odor
189 and/or reward-evoked suppression of PV neurons is modulated by changes in performance over the
190 course of a session (as performance changes with learning) or whether it is fixed within a session.
191 While these data establish relationships between behavior and PV neuronal activity across sessions,
192 we also sought to determine whether and how PV activity patterns were modulated over the course of
193 odor learning. To examine this, we first subdivided sessions into blocks, including the first 20 trials of an
194 odor pair, and best blocks, including the block of 20 trials with the highest accuracy in a session. As
195 expected, accuracy in the best blocks was consistently higher than accuracy in the first blocks, showing
196 that mice learned to discriminate novel odor pairs over the course of the sessions (**Figure 1L,** best
197 block – first block = 0.31 ± 0.02, $p < 0.0001$, $t = 18.99$, $df = 26$). Interestingly, we found that odor
198 evoked response peaks were not different between first and best blocks (**Figure 1M**). However, the
199 reward-evoked suppression of PV neuronal activity was significantly greater in the best blocks
200 compared to the first blocks (**Figure 1N, O**, best block – first block = -3.16 ± 0.84, $p < 0.001$, $t = 3.78$, df
201 = 26, paired t test). Together these findings indicate that the reward-related suppression of PV neurons,
202 but not odor response magnitudes, changed with learning.

203

204 ***SST neurons are excited by both odor presentation and reward delivery***

205 Within the BF, PV neurons receive inhibitory input from neighboring SST neurons. This disinhibitory
206 circuit contributes to the opposing effects that BF SST and PV neurons have on arousal state (Xu et al.,
207 2015). Given the nature of this connectivity, we next asked whether inhibition from SST neurons may
208 contribute to the reward-evoked suppression that we observed in PV neurons. To evaluate how SST
209 neurons selectively respond during odor discrimination learning, we again used fiber photometry during

210 the go/no-go task. For this, we selectively expressed GCaMP in BF SST neurons and implanted a
211 fiberoptic over the HDB (**Figure 2A, B**). As with PV-Cre, mice reliably learned S+/S- odor-reward
212 associations (d' = 1.75 ± 0.26, $p < 0.0001$, t = 6.65, df = 9, one-sample t test). Aligning the photometry
213 traces to odor port entry times revealed that SST neurons were excited by odor presentation (**Figure**
214 **2C**), and that this excitation was equivalent across trial types (**Figure 2D**, Hit = 1.39 ± 0.24, Miss = 1.46
215 ± 0.29, Correct Reject = 1.30 ± 0.20, False Alarm = 1.25 ± 0.23, p = 0.06, F = 3.85, df = 31, RM one-
216 way ANOVA). Responses were similar to what we observed in PV neurons upon odor presentation.
217 Notably, however, when traces were aligned to reward port entry (**Figure 2E**) we found that SST
218 neurons were also activated by reward delivery (**Figure 2F**, Hit AUC = 0.21 ± 0.13, False Alarm AUC =
219 -0.132 ± 0.14, $p < 0.01$, t = 5.16, df = 7, paired t test), in contrast to the suppression we observed in PV
220 neurons. These data show that SST and PV neurons in the HDB exhibit opposing responses to reward
221 delivery. Together, they support the hypothesis that SST and PV neurons serve opposing purposes in
222 go/no-go task reinforcement. This raises the question of how SST neuronal activity is correlated with
223 behavioral performance and decision-making, and to what extent the correlations oppose those
224 observed in PV neurons.

225 With the goal of directly comparing the two primary GABAergic neuronal subtypes in the HDB,
226 we examined correlations between the SST odor response magnitude, reward response magnitude,
227 behavioral performance, and decision making. In contrast to PV neurons, we found no correlation
228 between d' and SST odor response magnitude (Hit slope = 0.12 ± 0.10, r = 0.17, p = 0.23; Miss slope =
229 0.12 ± 0.14, r = 0.13, p = 0.38; Correct Reject slope = 0.09 ± 0.10, r = 0.12, p = 0.39; False Alarm slope
230 = 0.14 ± 0.11, r = 0.19, p = 0.19), nor did we observe differences between trial types in the relationship
231 between odor response magnitude and d' (slopes: p = .99, F = 0.04, df = 189, pooled slope = 0.12;
232 intercepts: p = 0.07, F = 2.43, df = 192, pooled intercept = 1.47). However, we found significant positive
233 correlations between odor response magnitude and response bias for Hit, Miss, and False Alarm Trials
234 (**Figure 2G,** Hit slope = 0.42 ± 0.16, r = 0.30, p < 0,05; Miss slope = 0.47 ± 0.18, r = 0.31, p < 0.01;
235 Correct Reject slope = 0.29 ± 0.16, r = 0.22, p = 0.07; False Alarm slope = 0.36 ± 0.17, r = 0.25, p <

236 0.05). The slopes and intercepts were not different between trial types (slopes: $p = .88$, $F = 0.22$, df =
237 273, pooled slope = 0.38; intercepts: $p = 0.26$, $F = 1.34$, df = 276, pooled intercept = 1.83). These data
238 imply that a larger odor-evoked response may be correlated with a more optimal decision bias (i.e.
239 closer to zero). However, without a substantial number of sessions with decision bias above zero, we
240 cannot determine whether the relationship would continue increasing linearly as criterion values
241 become suboptimal in the positive direction. Therefore, it remains a question whether larger S+ odor
242 responses in SST neurons are related to optimal decision-making behavior, or whether larger odor
243 responses reflect decision biases away from reward seeking behavior.

244 When traces were aligned to reward port entry, we found a slight negative correlation between
245 the magnitude of the reward-related response (AUC) and d' across sessions in Hit but not False Alarm
246 trials (Hit slope = -0.2 ± 0.09, $r = -0.37$, $p < 0.05$, False Alarm slope = 0.005 ± 0.09, $r = 0.01$, $p = 0.95$).
247 Taken together with our finding that reward-related excitation of SST neurons is larger in Hit trials than
248 in False Alarm trials, this analysis suggested that the difference between Hit and False Alarm trials was
249 greatest in sessions with lower overall d' values (indicating worse task performance). Comparing
250 reward response magnitudes to decision bias, we found no correlation between criterion and reward
251 response for Hits or False Alarms (Hit slope = -0.17 ± 0.17, $r = -0.14$, $p < 0.32$, False Alarm slope = -
252 0.14 ± 0.14, $r = -0.13$, $p = 0.34$). However, we did observe a significant difference between the
253 intercepts of the regressions for Hit vs. False Alarm trials (**Figure 2H,** Hit intercept = -0.02 ± 0.15, False
254 Alarm intercept = -0.24 ± 0.12, $p < 0.05$, $F = 5.60$, df = 109), confirming that increased reward
255 responses in Hit trials compared to False Alarms remained consistent across a range of decision
256 biases.

257 Next, to determine how patterns of SST neuronal activity were modulated during the learning of
258 a new S+/S- odor pair, we examined how odor and reward responses changed within go/no-go
259 sessions, as mice improved at the discrimination task. To examine performance-related changes, we
260 subdivided sessions into first blocks and best blocks (as described for PV neuronal recordings), with
261 first blocks showing significantly lower accuracy (**Figure 2I,** Best block – first block = 0.31 ± 0.02, $p <$

262 0.0001, t = 14.8, df = 30, paired t test). Aligning first and best block Hit trials to trial initiation revealed no
263 differences in odor-evoked peaks in SST neuronal activity (**Figure 2J**), suggesting that SST odor
264 responses are determined by the identity of the odor pair, and are not modulated by learning. However,
265 aligning Hit trials to reward port entry revealed a significant reduction in reward-related excitation of
266 SST neurons in the best blocks (Best Block AUC: -1.50 $\pm$ 0.48) compared to the first blocks (First Block
267 AUC: 1.305 $\pm$ 0.63, $p < 0.001$, t = 4.43, df = 30) (**Figure 2K, L**). Taken together with the negative
268 correlation between session average d' values and reward-related excitation (**Supplemental Figure**
269 **2C**), these data suggest that reward responses of SST neurons are modulated by performance, with
270 improvements in discrimination leading to a reduction in reward-related excitation both across odor
271 pairs with a range of difficulties, and within sessions, as mice learn to discriminate new S+ and S- odor
272 pairs.

273

274 ***DREADD-mediated inhibition of SST neurons does not impact firing of neighboring BF neurons***

275 We next sought to determine how directly manipulating BF GABAergic signaling impacted odor
276 discrimination and decision-making behavior. Towards this, we selectively expressed the inhibitory
277 DREADD hM4Di in BF SST neurons, first confirming that treatment with the DREADD ligand CNO
278 showed targeted and ligand-dependent inhibition (**Figure 3A-C**). We chose SST neurons for
279 manipulation because they have been shown previously to make local inhibitory synapses onto each of
280 the other major cell types within the HDB, including PV GABAergic, glutamatergic, and cholinergic
281 neurons (Zaborszky and Duque, 2000a; Xu et al., 2015). To determine the direct effect of CNO
282 treatment on hM4Di expressing SST neurons, we made acute brain slices harboring the HDB for whole
283 cell electrophysiological recordings. After current clamping mCherry labeled, hM4Di-expressing
284 neurons (**Figure 3D**) we made stepped current injections from -100 to 180 pA before and after CNO
285 application (10 μM). Prior to CNO, SST neurons showed fast-spiking patterns with narrow action
286 potentials as previously described (Anaclet et al., 2018) (**Figure 3E**). As expected, we found that CNO
287 significantly inhibited action potential firing in hM4Di expressing HDB SST neurons at current steps of

288 60 pA or greater (**Figure 3F**), though we did not observe systematic hyperpolarization with CNO (ΔVm -
289 2.18 ± 1.95, p = 0.33) (**Figure 3F, inset**). To examine whether inhibition of SST neurons impacted firing
290 properties of neighboring HDB neurons, we also patched and current clamped unlabeled, non-hM4Di-
291 expressing neurons (**Figure 3G**). Unlabeled neurons were slow spiking and susceptible to
292 depolarization block, suggesting that they represented cholinergic or glutamatergic subtypes (**Figure**
293 **3H**). We found that CNO treatment neither reduced, nor enhanced the firing of the non-hM4Di
294 expressing neurons in the HDB (**Figure 3I**). CNO application did, however, cause depolarization in non-
295 hM4Di-expressing neurons (ΔVm 3.22 ± 0.73, p < 0.01) (**Figure 3I, inset**). Notably, the observed
296 depolarization did not alter the overall firing properties of non-hM4Di-expressing neurons. While these
297 data indicate that reducing the ability of SST neurons to fire action potentials does not significantly
298 impact the ability of the other HDB neurons to fire action potentials when driven, they do not show how
299 DREADD-mediated inhibition of SST neurons impacts HDB circuit activity *in vivo* or during behavior.

300

301 ***DREADD inhibition of SST neurons modestly increases decision bias in go/no-go task***

302 To directly examine the role of BF SST neurons in odor discrimination and decision-making behavior,
303 we next selectively targeted hM4Di expression to BF SST neurons in the HDB, the magnocellular
304 preoptic nucleus (MCPO), and substantia innominata (SI) – regions forming a complex within the BF
305 that is densely interconnected with olfactory brain regions (Zheng et al., 2018) (**Figure 4A**). We then
306 trained mice on the go/no-go odor discrimination task and tested how they performed in sessions with
307 or without CNO treatment. In a subset of mice, mCherry instead of hM4Di-mCherry was selectively
308 expressed in SST neurons to serve as controls for CNO treatment. After training, mice were tested on
309 new S+/S- odor pairs for consecutive days until they either (1) successfully learned the new odor
310 associations (achieved two consecutive blocks of 85% accuracy), or (2) failed to meet the criteria for
311 learning three days in a row (**Figure 4B**). Odor pairs were then chosen to span a range of difficulties
312 and were approximately matched in difficulty between CNO and Vehicle treated sets of odors (Table 2
313 in methods). Mice were treated with either CNO (3.5 mg/kg) or Vehicle (1% DMSO in saline) for each

314 day of alternating odor pairs (**Figure 4B**). Sessions across multiple days of the same odor pair received
315 the same CNO or Vehicle treatment and were concatenated into single sessions from which sensitivity
316 and decision bias measures (d' and C) were calculated. Despite our earlier finding that discrimination
317 sensitivity was inversely correlated with reward related excitation in SST neurons, we found that
318 inhibiting SST neurons did not impact odor discrimination at the level of whole sessions (**Figure 4C,**
319 Hm4Di CNO-Vehicle = -0.06 $\pm$ 0.0.18, p = 0.74, t = 0.34, df = 7; Control CNO-Vehicle = 0.14 $\pm$ 0.0.19, p
320 = 0.49, t = 0.75, df = 5, paired t tests). Additionally, inhibiting SST neurons did not impact the rate at
321 which mice learned new odor associations (**Figure 4D**). These data suggest that odor and reward
322 evoked excitation of HDB SST neurons does not directly impact odor discrimination or odor
323 discrimination learning. Notably, however, we found that decision bias was subtly, but significantly
324 altered by CNO treatment in hM4Di expressing mice (**Figure 4E,** Hm4Di CNO-Vehicle = -0.11 $\pm$ 0.03, p
325 < 0.05, t = 3.38, df = 7; Control CNO-Vehicle = 0.04 $\pm$ 0.05, p = 0.47, t = 0.78, df = 5, paired t tests).
326 Thus, when HDB SST neurons were inhibited, mice showed a slightly stronger bias toward reward
327 seeking behavior (i.e. a more negative C value). This bias towards reward seeking moved decision-
328 making further away from the optimal decision bias of zero for our go/no-go task. Together, these data
329 suggest that HDB SST may affect reward-seeking without directly impacting odor discrimination or
330 learning in the context of a freely moving, self-initiated, go/no-go discrimination task.

331

332 ***Optogenetic manipulations of PV neurons influence odor discrimination but not decision bias***

333 To investigate the role of BF PV neurons in odor discrimination and decision-making, we targeted
334 conditional ChR2-GFP (AAV ef1a-Flex-hChR2-eYFP) to the BF neurons in the HDB of PV-cre mice and
335 placed fiber optic implants above the region to selectively activate the PV neurons (**Figure 5A-C**). Mice
336 were then trained on the go/no-go odor discrimination task while tethered to an optogenetic cable. After
337 training, mice received one of three optogenetic stimulation conditions during different go/no-go testing
338 sessions with novel S+/S- odor pairs (**Figure 5D, Table 3**). In the first condition, mice received 5
339 seconds of 20 Hz stimulation each time they received a reward on a Hit trial (**Figure 5D**, reward-locked

340 stimulation). In the second condition, mice received 5 seconds of 20 Hz stimulation every 20 seconds
341 regardless of where they were in a behavioral trial (**Figure 5D**, regular stimulation). In the last control
342 condition, mice were tethered to a fiberoptic cable but received no stimulation (**Figure 5D**, no
343 stimulation). Mice were randomized to different combinations of stimulus conditions and odor pairs.
344 Optogenetic stimulation time locked to reward delivery, during a time when PV neuronal activity is
345 typically suppressed (**Figure 1 G-J**), did not impact the overall accuracy of odor discrimination
346 compared to (**Figure 5E**, $p = 0.19$, $F = 1.97$, $df = 26$, RM one-way ANOVA). Optogenetic stimulation
347 also did not affect decision-bias, as C values across the three stimulation types showed no significant
348 difference (**Figure 5F,** $p = 0.14$, $F = 2.23$, $df = 26$, RM one-way ANOVA).

349 To determine the acute impact of BF PV neuronal activity on odor discrimination, we next targeted the
350 inhibitory light activated chloride channel iChloC (AAV-ef1a-Flex-iChloC-2A-dsRed) to BF PV neurons
351 (**Figure 5G-I**). We then placed bilateral fiberoptics over the HDB and trained mice to perform the go/no-
352 go task as described above. After training, mice received one of three optogenetic stimulation
353 conditions (**Figure 5J**) during different go/no-go testing sessions with the same set of S+/S- odor pairs
354 used in stimulation experiments (**Table 3**). In the first condition, mice received 500 ms of continuous
355 stimulation upon entering the odor port and triggering odor delivery on every trial (**Figure 5J**, All). In the
356 second condition, mice received 500 ms of continuous stimulation on 50% of the trials selected at
357 random (**Figure 5J,** Random). In the third condition, mice received 500 ms of continuous stimulation
358 every 20 seconds regardless, analogous to the "regular stimulation" condition for optogenetic
359 stimulation (**Figure 5J**, Control). Mice were randomized to different combinations of stimulus conditions
360 and odor pairs. Surprisingly, we found that optogenetically inhibiting BF PV neurons during all odor
361 presentations within a session improved odor discrimination (**Figure 5K**). D' values were significantly
362 higher in sessions where BF PV neurons were inhibited during all odor presentations compared to
363 sessions where only 50% of trials triggered inhibition and sessions where inhibition was not time-locked
364 to odor presentations ($p < 0.01$, $F = 11.8$, $df = 14$, RM one-way ANOVA). Inhibition of BF PV neurons
365 did not, however, affect decision-bias (**Figure 5L,** $p = 0.35$, $F = 1.18$, $df = 14$, RM one-way ANOVA)

366 indicating that the reduction in errors was balanced across miss and false alarm-type errors. Together,
367 these results highlight distinct roles for different BF GABAergic neuronal subtypes in different aspects
368 of odor discrimination behavior including odor discrimination and decision making.

369

370 **DISCUSSION**

371 Particular attention has been paid to the role of BF cholinergic neurons in regulating behavioral
372 state. BF cholinergic neurons mediate effects of attention and arousal at downstream circuits, and are
373 disproportionately affected by neurodegenerative diseases like Alzheimer's and Parkinson's (Sarter and
374 Bruno, 1997; Levin and Simon, 1998; Sarter et al., 2001; Grothe et al., 2010; Parrao et al., 2012). BF
375 cholinergic neurons respond directly to sensory cues, positive and negative reinforcement during
376 learning, and changes in behavioral states across multiple timescales (Phillis, 1968; Szymusiak, 1995;
377 Sarter and Bruno, 1999; Hasselmo and McGaughy, 2004; Parikh et al., 2007; Chaudhury et al., 2009;
378 Hangya et al., 2015; Xu et al., 2015; Ruivo et al., 2017; Patel et al., 2019). Activity of non-cholinergic
379 neurons in the BF is also strongly correlated with behavioral state, sensory perception, and
380 performance on behavioral tasks (Hassani et al., 2009; Devore et al., 2015; Hangya et al., 2015; Xu et
381 al., 2015; Harrison et al., 2016). Previous studies using auditory, visual, and olfactory cues have found
382 increased activity in BF neurons in response to conditioned stimuli, positive and negative
383 reinforcement, and in anticipation of salient stimuli (Lin and Nicolelis, 2008; Hangya et al., 2015; Zheng
384 et al., 2018; Nunez-Parra et al., 2020). BF neuronal activity is also modulated by expectation, with more
385 surprising reinforcement eliciting larger increases in firing for both cholinergic (Hangya et al., 2015) and
386 non-cholinergic BF neurons (Lin and Nicolelis, 2008; Zheng et al., 2018).

387 In the context of the olfactory system, BF cholinergic and GABAergic neurons send extensive
388 projections to the olfactory bulb (OB) (Zaborszky et al., 1986). GABAergic projections preferentially
389 target specific GABAergic interneurons in the OB, where they influence fine odor discrimination, signal
390 to noise ratios, and the survival of adult born neurons (Böhm et al., 2020; Hanson et al., 2020; de Saint
391 Jan, 2022). A direct comparison of the impact of BF cholinergic and GABAergic projections on OB

activity reveals that BF GABAergic neurons preferentially increase odor-evoked mitral cell firing and suppress spontaneous activity, while cholinergic neurons increase spontaneous, sniff-locked, and odor evoked mitral cell firing (Böhm et al., 2020). In olfactory tasks, both cholinergic and non-cholinergic BF neurons respond to conditioned stimuli, unconditioned stimuli, and both positive and negative reinforcement (Hangya et al., 2015; Nunez-Parra et al., 2020; Hanson et al., 2021), with a significant proportion of BF neurons showing suppression in response to odor stimuli and positive reinforcement (Nunez-Parra et al., 2020). Additionally, we have recently shown that BF GABAergic activity is powerfully suppressed after positive reinforcement (Hanson et al., 2021). Previous studies, however, did not differentiate between subtypes of non-cholinergic neurons and were, therefore, unable to discern distinct roles of BF GABAergic neuronal subtypes on odor-guided behavior.

Here, we separately targeted PV and SST GABAergic neurons in the BF, with the goal of determining how they uniquely contribute to BF olfactory discrimination, learning, and decision-making behavior. We showed that, while both neuronal subtypes are excited by odor stimuli, each subtype responds in opposite ways to positive reinforcement. Specifically, SST neurons were briefly excited by reward delivery, while PV neurons showed a sustained suppression after obtaining a reward. The opposite responses of PV and SST neurons to reinforcement mirrors the opposing roles of PV and SST neurons in behavioral state regulation. While opposing responses in PV and SST populations may be driven, in part, by direct inhibition of PV neurons by SST neurons in the BF, the congruency of their responses to odor stimuli suggest that this relationship is more complicated. It is possible, for example, that the inhibitory input from SST to PV neurons is gated differently in response to external sensory inputs than it is for internal state and/or reinforcement information. While our findings do not suggest specific gating mechanisms, they do reveal a clear divergence in how BF circuits encode sensory inputs and reinforcement feedback.

The opposing responses of PV and SST neurons to reward delivery are intriguing because they mirror the opposite responses of BF GABAergic neurons to changes in behavioral state (Xu et al., 2015; Harrison et al., 2016). This suggests that the two cell types play distinct roles in the response to

418 positive reinforcement during discrimination learning, though whether each cell type's activity impacts
419 discrimination or alters decision making is not clear. Correlating the magnitude of each cell type's
420 reward-related responses to discrimination sensitivity and decision bias provides insight into their
421 potential roles, if not information about causal mechanisms. Importantly, correlations observed between
422 neuronal activity and behavioral performance may be due to neuronal activity causing behavioral
423 changes, behavioral changes causing changes in BF neuronal activity, or a larger contextual or state
424 change impacting both neuronal activity and behavior. SST neurons are intriguing components of the
425 BF circuit because they directly inhibit each of the other major cell types in the BF, including
426 glutamatergic, cholinergic, and PV GABAergic neurons. Notably, these previously described patterns of
427 synaptic connectivity in the BF were revealed with optogenetic circuit mapping. In all its utility,
428 optogenetic circuit mapping leverages artificial, channel rhodopsin-mediated stimulation of SST
429 neurons and, thus, does not indicate the extent to which SST synapses affect the activity of
430 downstream BF neurons during normal circuit activity. To help better determine the impact of SST
431 neuronal excitability on other cell types of the BF, we expressed an inhibitory DREADD in SST neurons
432 and measured action potential firing and resting membrane potentials in both DREADD and non-
433 DREADD expressing neurons. While CNO treatment effectively inhibited action potential firing of SST
434 neurons driven by current injections, it did not systematically alter action potential firing in neighboring
435 non-DREADD expressing neurons. However, CNO treatment did lead to a slight increase in the resting
436 membrane potential of non-DREADD expressing neurons. This suggests that SST neurons may be
437 tonically inhibiting neighboring BF neurons, and that DREADD-mediated inhibition of SST neurons
438 relieves some of this inhibition, raising the resting potential of neighboring neurons.

439 To investigate whether SST neuronal activity was driving behavioral changes, as suggested by
440 the correlation analysis, we chemogenetically inhibited SST neurons during a subset of go/no-go
441 testing sessions. Based on our observed correlations, we predicted that (1) if SST excitation during
442 odor exposure was driving more optimal decision-making behavior, then inhibiting SST neurons would
443 lead to larger (more negative) decision biases, (2) if higher reward-related excitation of SST neurons

444 was causing poor discrimination, then inhibiting SST neurons would improve sensitivity, and (3) if a
445 reduction in SST reward-related excitation facilitated learning, then inhibiting SST neurons would
446 increase the rate at which discrimination sensitivity (d') improved within sessions. Comparing go/no-go
447 discrimination testing sessions in which BF SST neurons were chemogenetically inhibited to sessions
448 in which BF SST neurons were not inhibited, we found that DREADD-mediated inhibition of SST
449 neurons led to a modest reduction in criterion scores with no change in discrimination within or across
450 sessions. Together, these data suggest that SST neuronal activity influences reward-seeking behavior
451 without altering discrimination ability or discrimination learning directly.

452 Finally, to investigate whether PV neuronal was driving decision-making behavior or influencing
453 odor discrimination, we incorporated optogenetic manipulations of BF PV neurons into the go/no-go
454 assay. Although we had previously found that suppression of PV neuronal activity was correlated with
455 reward delivery, optogenetic stimulation of the BF PV neurons in the post-reward period did not affect
456 either decision-bias or odor discrimination. Instead, optogenetic inhibition of PV neurons during odor
457 presentations (blunting the odor-evoked peak in BF PV neuronal activity) effectively increased session
458 accuracy without affecting decision bias. These data indicate that inhibiting BF PV neurons during odor
459 presentations improves odor discrimination, and they agree with the negative correlation we observed
460 between odor response peak magnitudes and session d' averages (**Figure 1I**). Together, these results
461 suggest that BF PV activity likely has a direct, causal impact on odor discrimination.

462 In conclusion, our findings highlight unique activity patterns exhibited by BF GABAergic PV and
463 SST neurons in response to olfactory stimuli and reward reinforcement, and provide valuable insights
464 into the processing of odor and reward information within the BF. Our results underscore the nuanced
465 contributions of distinct BF GABAergic neuronal subtypes to the complex landscape of odor-guided
466 decision-making behavior. Together, this work advances our understanding of the neural mechanisms
467 underlying sensory perception and decision-making processes and sheds light on the multifaceted role
468 played by specific neuronal subpopulations in the BF.

469

470 **MATERIALS AND METHODS**

471 ***Mice***

472 Mice were maintained on a 12-h light-dark cycle and were treated in compliance with the ethical
473 guidelines of the US Department of Health and Human Services and approved by IACUC at Baylor
474 College of Medicine. Both male and female mice over 2 months of age were included for all
475 experiments. SST-Cre (JAX#: 13044) and PV-Cre (JAX#: 17320) mice were originally purchased from
476 Jackson Laboratories.

477

478 ***Surgery and viral constructs***

479 Surgical procedures were performed under general anesthesia using isoflurane (4% v/v) induction and
480 maintained under isoflurane with O2 (1-2% v/v) inhalation. Following anesthetic induction, mice were
481 secured to a stereotaxic frame and administered 5 mg/kg of meloxicam prior to surgery. All procedures
482 were carried out using to Angle 2 software (Leica Biosystems) to set and locate coordinates.
483 Craniotomies were performed over the horizontal diagonal band of Broca (HDB) at the coordinates from
484 Bregma: ML +/- 1 mm; AP 0.7 mm; DV -5.4 mm. For fiber photometry, to target the HDB for viral
485 expression of calcium-indicator GCaMP6f, cohorts of PV-Cre (N = 6) and SST-Cre (N = 8) mice were
486 unilaterally injected with 250 nL of AAV2/9 hSyn-Flex-GCaMP8s-WPRE. Following viral injection, a
487 custom fiber optic implant (0.48 na, 200 um core diameter, RWD systems) was placed so that the tip of
488 the fiberoptic was 0.1 mm dorsal to the HDB coordinates used for viral injection. Implants were then fixed
489 with Metabond dental cement (Parkell).

490 For optogenetic stimulation, PV-Cre mice (N = 6) were bilaterally injected with 250 nL of AAV-Efla-DIO-
491 ChR2(h134R)::EYFP-WPRE-pA (serotype DJ8) at the same coordinates. For optogenetic inhibition, PV-
492 Cre mice (N = 5) were injected at the same coordinates with 250 nL of AAV-ef1a-Flex-iChloC-2A-dsRed
493 (Addgene plasmid: 70762, serotype DJ8, packaged by the BCM Neuroconnectivity Core). Following viral
494 injection, the same fiber optic implants used for photometry were inserted, bilaterally at 5-degree angles

495 and placed so that the tips of the fiberoptics were 0.3 mm dorsal to the HDB coordinates used for viral
496 injection. Implants were then fixed with Metabond dental cement (Parkell).

497 For inhibitory DREADD expression, SST-Cre mice were bilaterally injected with 250 nL of AAV-DIO-
498 hM4Di-mCherry (N = 8) or AAV-DIO-mCherry (N = 6) at the same HDB coordinates. All mice were given
499 a 2-week recovery period prior to the start of behavioral testing. HDB/MCPO/SI targeting was verified in
500 all cases with post hoc immunofluorescence imaging of viral expression.

501

502 ***Go/no-go training***

503 Freely moving mice were trained on an olfactory-cued go/no-go discrimination task using olfactory
504 conditioning boxes (Med Associates) controlled by MedPC software. Conditioning boxes included one
505 odor delivery port and one water reward port, both equipped with IR beams to record port entries. The
506 odor delivery port received a constant stream of clean room air, cleared by a vacuum. Odors (Sigma,
507 Tables 1-3) were injected into the steady air stream by opening valves to one of two odor reservoirs,
508 allowing the air stream to pass through the head space of the reservoir carrying the volatized odorant.
509 Reservoirs were 20 mL in volume and included 2.5 mL of odorant diluted to 1% by volume in mineral oil.
510 Water rewards were dispensed at 5uL in volume in the separate reward port upon reward port entry only
511 on correctly decided Hit trials. Conditioning boxes were housed within larger behavior isolation boxes
512 (Med Associates). Box fans in the isolation boxes continuously circulated ambient air away from the
513 conditioning boxes and out of the isolation boxes to reduce the accumulation of ambient odor.

514 Over the course of 10-14 days, mice underwent 5 stages of behavior-shaping as previously
515 described (Hanson et al., 2021). Mice were water restricted to no less than 85% of their body weight
516 during the 48 hours prior to the start of training. Mice were first trained to seek water rewards, then to
517 initiate trials by poking their nose into the odor port. Mice were then trained to respond to an S+ odor cue
518 (1% Eugenol in mineral oil) to receive a water reward. Upon forming this association, the S- odor cue
519 (1% Methylsalicylate in mineral oil) was introduced, in which mice were trained to refrain from seeking a
520 reward and instead initiate another trial. Trials required mice to sample the odor cues for 100ms or more

521 before responding to the cue and were categorized based on the S+/- odor cue and the mouse's
522 response. When mice were presented with the S+ odor cue, trials were considered "Hits" when mice
523 sought a water reward within 5s and "Misses" if mice did not enter the reward port. Trials in which the S-
524 odor cue was delivered were considered "False Alarms" when mice incorrectly attempted to retrieve water
525 and "Correct Rejects" if mice did not seek water. False alarms resulted in a 4-second time out
526 punishment. Accuracy was calculated as percent correct trials (hit + correct reject trials) for blocks of 20
527 trials. For each training session, mice completed 10-20 blocks. Training was considered complete after
528 mice completed a session with the training odors (Eugenol = S+, Methysalicylate = S-) in which they
529 achieved higher than 85% accuracy in at least 2 consecutive blocks. Testing sessions followed the same
530 pattern as the last stage of training, but new odor pairs were introduced, requiring mice to learn new S+
531 and S- odor associations (Tables 1-3).

532

533 ***Go/no-go testing with fiber photometry***

534 For go/no-go testing with concurrent photometry mice were attached to a fiberoptic cable, connected to
535 a two-channel fiber photometry recording system (Doric) via a rotary joint in the top of the behavior box.
536 Odor pairs for photometry experiments were chosen randomly for each mouse and session from the list
537 in Table 1 so that each odor was never presented on more than one day. The timing of trial initiations
538 and reward port entries were measured by IR beams in the odor and reward ports. Port entry timings,
539 odor presentations, and trial outcomes were recorded with (Med Associates). The timing of each odor
540 presentation was output to the photometry recording system as a TTL pulse lasting the duration of an
541 odor presentation allowing synchronization of the photometry and behavior. Sessions were excluded if
542 mice failed to complete at least 100 trials and if the average d' value across the whole session was less
543 than 0.25.

544

545 **Table 1: Odors used in go/no-go experiments with fiber photometry**

Odor	Molecular Weight (g/mol)	Vapor Pressure (mmHg)	Functional Group	Cat. Number
Isovaleric Acid	102.13	0.44	Carboxylic acid 5C	31024
(+) Carvone	150.22	0.16	Cyclic ketone 10C 1 double bond	124931
(-) Carvone	150.22	0.16	Cyclic ketone 10C 1 double bond	22070
1-Methylpyrrole	81.12	15.00	Cyclic nitrogen	509973
Acetophenone	120.15	0.40	Aromatic ketone	200905
Guaiacol	124.14	0.10	Aromatic ether, alcohol	253200
P-Toyl Acetate	150.17	0.16	Aromatic ester, 7C	307300
Amyl Acetate	130.00	4.00	Ester 7C	504009
1-Octen-3-ol	128.22	0.53	Alcohol, 8C	280518
(+) Limonene	136.23	2.00	Cyclic 10C 2 double bond	183164
(-) Limonene	136.23	2.00	Cyclic 10C 2 double bond	218367
Benzaldehyde	106.12	1.00	Aromatic aldehyde	B1334
Isoamyl Acetate	130.19	4.00	Ester 7C	205508
1,4-Cineole	154.25	1.93	Cyclic oxygen, ether	27393
2-Methypyrazine	94.12	9.69	Pyrazine	75608
2-Ethylphenol	122.16	0.15	Aromatic alcohol	44000
Citral	152.24	0.22	Aldehyde	83007
2,6 Dimethyl-5-heptenal	140.22	0.62	Aldehyde, 8C	238902
alpha-Pinene	136.24	3.00	Cyclic 7C 1 double bond	147524
Cyclohexanol	100.16	0.66	Cyclic alcohol	105899
Allyl Sulfide	114.00	9.22	Sulfide	A35801
1-Butenol	74.12	7.00	Alcohol, 4C	281549
1-Pentanol	88.15	44.6	Alcohol, 5C	138975
2-Heptanol	116.20	1.00	Alcohol, 7C	328804
1-Hexanol	102.18	1.00	Alcohol 6C	H13303
1-Heptanol	116.20	0.22	Alcohol 7C	H2805

1-Octanol	130.23	0.14	Alcohol 8C	297887
Butylbenzene	134.22	1.03	Aromatic 10C	686859
Cyclobutanecarboxylic Acid	100.12	0.18	Cyclic carboxylic acid 5C	C95609
P-Cymene	134.21	1.50	Aromatic 10C	30039
Decane	142.29	1.43	Hydrocarbon	30540
Diethylbenzene	134.22	1.03	Aromatic 10C	D91055
2,3-Hexanendione	114.14	10.00	Ketone, 6C	255801
alpha-Phellandrene	136.24	1.86	Cyclic 10C 2 double bond	285609
Isoamyl Butyrate	158.00	0.95	Ester 9C	206008
Menthone	154.00	0.50	Cyclic ketone 10C	218235
2-Heptanone	114.18	3.00	Ketone 7C	537683
Anisole	108.00	3.54	Aromatic ether	123226

Fiber optic cables (0.48 na, 400 um core diameter) connected light emitting diodes (465 nm experimental and 405 nm isosbestic excitation wavelengths) to a filter cube that separating excitation and emission wavelengths (Doric). Excitation wavelengths were directed along a fiber optic tether (0.48 na, 200 um core diameter) toward the mouse through a rotary connector attached to the behavior box. The same fiber carried emission wavelengths from the mouse to the filter cube, which was then directed to a femtowatt photodetector (Newport) through a fiber optic cable (0.48 na, 600 um core diameter). 405 and 465 nm excitations were controlled by Doric Studio software in “lock-in” mode and the emission evoked by each channel was separated into distinct Ca^{2+}-dependent and isosbestic GCaMP traces in Doric Studio. Traces were then exported to MATLAB where Ca^{2+}-dependent GCaMP traces were scaled to the isosbestic traces, isosbestic signals were subtracted to remove artifacts, and the subtracted traces were z-scored. Signals were then aligned to odor presentations and subdivided into individual go/no-go trials using the TTL output from the behavior apparatus.

Z-scored photometry traces from individual trials within a go/no-go session were sorted based on trial type and outcome. Additional realignment of photometry traces based on reward port entry time was

561 carried out in MATLAB using output from MedPC software. Mean traces were calculated for each session
562 by trial type and averaged across animals and sessions. Error was calculated as the 95% confidence
563 interval across sessions. Peak odor response values were calculated as the maximum value of the z-
564 scored photometry trace during the odor presentations on individual trials and then averaged across the
565 session. Session averages were then averaged for each animal and mouse-averaged values were
566 compared across trial types using one way ANOVA. For photometric recordings of GCaMP from SST
567 neurons, the area under the curve (AUC) of the reward-related response was calculated for Hit and False
568 Alarm traces by summing the z score from reward port entry to 1 second after reward port entry. For
569 recordings from PV neurons, reward-related suppression was calculated as the sum of the z-scored trace
570 from reward port entry to 5 seconds after reward port entry. Values were not calculated for Miss and
571 Correct Reject trials because those trials did not involve reward port entry. For analyses subdividing
572 sessions to examine within-session learning (**Figure 1L-O, Figure 2I-L**), traces were extracted from
573 single blocks of 20 trials. The "first block" included the first 20 trials from a session. The "best block" was
574 considered the block of 20 trials with the highest accuracy. If more than one block achieved the same
575 level of high accuracy, traces from the first instance of high accuracy were used. AUC values were then
576 calculated from Hit trials within the "first block" and the "best block" of a session and compared with a
577 paired t-test.

578

579 ***Go/no-go testing with chemogenetic and optogenetic manipulations***

580 For go/no-go experiments involving DREADD mediated inhibition of SST neurons, odor pairs were
581 presented in the order shown in Table 2. The same odor pairs were presented on consecutive days until
582 mice achieved at least two consecutive blocks of 85% accuracy, when the odor pair was considered
583 learned, or until the mice failed to learn for three consecutive days. Sessions of the same odor pair were
584 then concatenated into a single session spanning up to three days. Concatenated sessions were
585 excluded from analysis if mice failed to complete at least 100 trials. Mice were treated each day, 15
586 minutes before starting the go/no-go task, with either CNO (3.5 mg/kg in 1% DMSO, Tocris) or vehicle

587 (1% DMSO in saline) by I. P. injection. Mice were habituated to I. P. injections of 1% DMSO during the
588 last stage of go/no-go training. CNO or vehicle treatment was consistent within each concatenated
589 session such that each session of the same odor pair (up to three consecutive sessions) was associated
590 with the same drug treatment (**Figure 4B**). As an additional control, a subset of mice was injected with a
591 non-DREADD expressing virus (AAV-ef1a-FLEX-mCherry) and subjected to the same experimental
592 paradigm.

593 For go/no-go testing with optogenetics stimulation of PV neurons, PV-Cre mice injected with
594 conditional ChR2 and implanted with fiberoptics were attached to a bifurcated fiber optic cable attached
595 to commutator at the top of the experimental box that connected to a Doric 473 nm laser. The laser was,
596 in turn, connected to an AMPI Master-8 pulse stimulator that cued the laser to pulse at 20 Hz for 10 ms
597 based on either internal programming or specific behavioral inputs from the mice, depending on the
598 stimulation condition. Laser power was modulated so that the output of the fiber connecting to the
599 fiberoptic implant was 2 mW. Behavioral sessions were run once per day on weekdays. Each session,
600 mice performed the go/no-go behavioral task using one of 12 novel S+/S- odor pairs (**Table 3**). Each
601 session corresponded to one of three different stimulation conditions randomized across sessions and
602 mice so that different mice received different combinations of odor pairs and stimulation conditions. In
603 the “reward-locked stimulation” experimental condition, reward delivery triggered the onset of a 5 second
604 burst of 20 Hz laser light stimulation. In the “regular stimulation” control condition, 5 second pulses of 20
605 Hz laser light were triggered every 20 seconds regardless of the state of mouse in the behavioral task.
606 In the “no stimulation” control condition, mice were tethered to the bilateral fiberoptic, but no laser light
607 was delivered. Each mouse underwent multiple sessions of all three conditions but was only exposed to
608 each odor pair once.

609 For go/no-go testing with optogenetics inhibition of PV neurons, PV-Cre mice were injected with
610 conditional iChloC and implanted with fiberoptics then attached to a bifurcated fiber optic cable and
611 commutator that connected to a Doric 473 nm laser as for optogenetic stimulation. For iChloc
612 experiments, an AMPI Master-8 pulse stimulator cued the laser to output a single 500 ms duration pulse

613 based on either internal programming or specific behavioral inputs from the mice, depending on the
614 stimulation condition. Behavioral sessions were run once per day on weekdays. Each session, mice
615 performed the go/no-go behavior task using one of 12 novel S+/S- odor pairs (**Table 3**), similar to
616 optogenetic stimulation experiments. Each session corresponded to one of three different stimulation
617 conditions randomized across sessions and mice so that different mice received different combinations
618 of odor pairs and stimulation conditions. In the "all trials" experimental condition, odor presentations
619 triggered the onset of the 500 ms pulse of laser light. In the "random trials" odor presentations triggered
620 laser pulses 50% of the time at random. In the control condition, 500 ms pulses of laser light were
621 delivered every 20 seconds regardless of the state of the mouse in the behavioral task. Each mouse
622 underwent multiple sessions of the three conditions but was only exposed to each odor pair once.

623 **Table 2: Odors used in go/no-go experiments with DREADD-mediated inhibition of SST neurons**

Pair #	*Odor*	*S+/S-*	*Treatment*	*Cat. Number*
1	Anisole Acetophenone	S+ S-	Vehicle	123226 200905
2	Isoamyl Acetate 2-Heptanone	S+ S-	CNO	205508 537683
3	2-Methypyrazine alpha-Pinene	S+ S-	Vehicle	75608 147524
4	(+) Carvone (-) Carvone	S+ S-	CNO	124931 22070
5	(+) Limonene (-) Limonene	S+ S-	Vehicle	183164 218367
6	2-Ethylphenol 1,4-Cineole	S+ S-	CNO	44000 27393
7	1-Butenol 1-Pentanol	S+ S-	Vehicle	281549 138975
8	1-Hexanol	S+	CNO	H13303

	1-Heptanol	S-		H2805
9	2,3 Hexanendione Citral	S+ S-	Vehicle	255801 83007
10	Isoamyl Butyrate Menthone	S+ S-	CNO	206008 218235

624

625 **Table 3: Odors used in go/no-go experiments with optogenetic stimulation and inhibition of PV**

626 **neurons**

Pair #	*Odor*	*S+/S-*	*Cat. Number*
1	Acetophenone Anisole	S+ S-	200905 123226
2	Isoamyl Acetate Isoamyl Butyrate	S+ S-	205508 206008
3	(+) Carvone (-) Carvone	S+ S-	124931 22070
4	(+) Limonene (-) Limonene	S+ S-	183164 218367
5	2-Ethylphenol 1,4-Cineole	S+ S-	44000 27393
6	2-Heptanone Menthone	S+ S-	537683 218235
7	2,3 Hexanendione Citral	S+ S-	255801 83007
8	2-Methypyrazine alpha-Pinene	S+ S-	75608 147524
9	1-Butanol 1-Pentanol	S+ S-	281549 138975
10	1-Hexanol	S+	H13303

	1-Heptanol	S-	H2805
11	Guaiacol Eucalyptol	S+ S-	253200 246506
12	Trans-cinnamaldehyde Methyl Acetate	S+ S-	239968 296996

627

628 ***Quantification of go/no-go task performance***

629 Go/no-go task performance was quantified using the signal detection theory measures d prime ($d' =$
630 $Z(Hit\ Rate) - Z(False\ Alarm\ Rate)$) and criterion ($C = -1(Z(Hit\ Rate) + Z(False\ Alarm\ Rate))$)
631 (Stanislaw and Todorov, 1999). d' measures the sensitivity of discrimination and reflects overall task
632 performance. C measures discrimination bias. More negative C values reflect a bias towards reward
633 seeking, values close to 0 reflect optimal decision bias, and positive values reflect bias away from reward-
634 seeking, in favor of trial reinitiation. To show change in sensitivity over time within a session, d' was
635 calculated over a rolling window of 40 trials. Session summary d' values were calculated as the maximum
636 d' over a 40-trial rolling window. This was done to avoid early trials where mice were learning new S+
637 and S- associations and later trials where mice may have disengaged with the task. For experimental
638 and control mice in SST DREADD inhibition experiments, d' and C were calculated for each odor pair
639 and values were averaged for each mouse separated by treatment condition. Mean values for each
640 mouse from CNO treatment sessions were compared to mean values from vehicle treatment sessions
641 by paired t-tests. For optogenetic stimulation and inhibition experiments, d' and C were calculated for
642 each odor pair and values were averaged for each mouse separated by stimulation conditions.
643 Stimulation conditions were then compared using repeated measures one-way ANOVA and Tukey
644 corrections for multiple comparisons.

645

646 ***Electrophysiology***

647 For slice electrophysiological recording experiments, mice (N = 3) were deeply anesthetized with
648 isoflurane then transcardially perfused with ice-cold artificial cerebrospinal fluid (aCSF) solution
649 containing (in mM): 125 NaCl, 2.5 KCl, 1.25 NaH2P04, 1 MgCl2, 2 CaCl2, 25 glucose, and 25
650 bicarbonate (pH 7.3, 295 mOsM). Brains were removed and transferred into ice-cold cutting solution
651 containing (in mM): 2.5 KCl, 1.25 NaH2PO4, 10 MgSO4, 0.5 CaCl2, 234 sucrose, 11 glucose, and 26
652 bicarbonate. Cutting solution was continuously bubbled with 95% CO2 / 5% O2. Brains were mounted
653 with cyanoacrylate glue and immediately submerged in oxygenated cutting solution on a Leica VT1200
654 vibratome. 300 um coronal sections were made at a cutting speed of 0.1 mm/s. Slices including the
655 HDB were removed to a slice recovery chamber of oxygenated aCSF at 37C for at least 30 minutes.
656 Following recovery, slices were slowly returned to room temperature for 30 minutes before recording.

657 For whole-cell current clamp recordings, slices were submerged in a recording chamber and
658 continuously perfused with room temperature oxygenated aCSF at ~2 mL/minute. Cells were visualized
659 with DIC optics (Olympus BX50WI) and fluorescence imaging (Q Capture). Once visualized, cells were
660 whole-cell patched in current-clamp configuration. Recording electrodes (3–7 megaohms) were pulled
661 from thin-walled borosilicate glass capillaries (inner diameter: 1.1 mm, outer diameter: 1.5 mm) with a
662 horizontal micropipette puller (Sutter Instruments). Current-clamp internal solution contained (in mM):
663 120 K gluconate, 20 HEPES, 10 EGTA, 2 MgATP, and 0.2 NaGTP (with 0.4% biocytin by weight, pH to
664 7.3 with KOH, 285 mOsM). Recordings were made using PClamp software (Axon) with an Axon
665 MultiClamp 700B amplifier digitized at 10 kHz (Axon Digidata 1440A). Once a whole cell patch was
666 achieved, cells were allowed to equilibrate for five minutes before resting membrane potential was
667 recorded and current injections were performed. Cells were then injected with 1 s current steps from -
668 100 pA to +180 pA in intervals of 20 pA. Resting membrane potential was recorded and current
669 injections were repeated three times. After recording current injections at baseline, CNO (10 uM) was
670 washed added to the bath and allowed to circulate for 10 minutes. Resting membrane potential was
671 recorded and current injections were repeated three times in the presence of CNO. During all
672 recordings, access resistance was continuously monitored, and cells where the access resistance

673 changed by more than 20% were excluded from analysis. N = 5 fluorescently labeled cells and N = 7
674 unlabeled cells. Traces were then exported to MATLAB where resting membrane potential and spike
675 counts were calculated with custom scripts.

676 All cells were dialyzed with 0.4% biocytin for the duration of the recording and patched neurons
677 were saved for post hoc imaging. After recordings, electrodes were withdrawn slowly allowing the cells
678 to reseal and form an outside-out patch. Slices were then allowed to equilibrate in the recording
679 chamber for 5 minutes before being transferred to 4% PFA. After patching and cell-filling, slices were
680 fixed overnight in 4% PFA at 4º C. Slices were then washed 3x in 0.1% PBS-T for 30 min each. After
681 washing, slices were incubated in 10% normal goat serum blocking buffer for 2 hours at room
682 temperature. Slices were then incubated in streptavidin conjugated to Alexa:647 (1:500, Invitrogen)
683 overnight at 4C. The next day, slices were washed 3x in 0.1% PBS-T for 30 min, then mounted on
684 glass slides using 500 um spacers (Electron Microscopy Sciences) filled with mounting media without
685 DAPI (Southern Biotech). Slices were imaged on a Leica SP8 confocal with a 20x objective to verify
686 colocalization with DREADD expression. Z stacks of filled cells were reconstructed in FIJI.

687

688 ***Immunofluorescence and imaging***

689 For antibody staining of GCaMP in mice used for photometry experiments, mice were deeply
690 anesthetized then transcardially perfused with PBS followed by 4% PFA. Brains were removed and
691 immersion fixed in 4% PFA overnight at 4C. Brains were transferred to 30% sucrose and allowed to
692 equilibrate, then they were frozen and sectioned at 40 um on a cryostat (Leica). Sections were washed
693 in 0.3% PBS-T, then incubated in a blocking solution composed of 10% normal goat serum, 0.3% PBS-
694 T, and 3M glycine for 1 hour at room temperature. Following blocking, slices were incubated in primary
695 antibody (Chicken a GFP, 1:1000, Abcam, ab13970) diluted in blocking buffer overnight at 4C. The next
696 day slices were washed 3x in 0.1% PBS-T then incubated in secondary antibody (Goat a Chicken:488,
697 1:1000, Invitrogen, A32931) for 2 hours at room temperature. Slices were then washed 3x in 0.3%
698 PBS-T, transferred to 0.5x PBS, and mounted on glass slides with DAPI-containing mounting media

699 (Southern Biotech). For fluorescence imaging of DREADD-mCherry and iChloC-dsRed expression, the
700 endogenous mCherry and dsRed fluorescence was sufficient for imaging and no antibody staining was
701 performed. Sections were imaged on a Leica DM6000B epifluorescence microscope. For
702 characterization of DREADD expression in mice used for behavioral experiments (**Figure 4**), three
703 equivalent sections including the HDB/MCPO/SI complex were selected from each mouse and the
704 region of viral expression was outlined manually in FIJI and superimposed onto the matching coronal
705 section schematic (**Figure 4A**).

706

707 ***Experimental Design and Statistical Analyses***

708 All statical analyses were caried out in Prism (Graphpad). Tests performed along with relevant F, t, and
709 degrees of freedom are reported in the text. For insignificant comparisons, exact p values are reported.
710 Significant p values are reported as $p < 0.5$, 0.01, 0.001, or 0.0001 as appropriate. Errors reported in
711 the text are SEM unless otherwise noted. For comparisons across four trial types where values were
712 matched by animal and session, repeated measures one-way ANOVAs were used with Tukey
713 corrections for multiple comparisons. For comparisons across two trial types or groups where values
714 were matched by animal and session, paired t tests were used. For comparisons to a null hypothesis
715 value, one sample t tests were used. When mouse average values are reported, overall averages and
716 errors are calculated from mouse average values. For correlation analyses, correlations are reported as
717 Pearson's R values. Lines of best fit, confidence intervals, slopes, intercepts, and significance values in
718 were calculated with simple linear regressions. For analyses comparing CNO and vehicle treatment in
719 control and experimental animals paired t tests were performed separately for control and experimental
720 mice to compare CNO to vehicle treated sessions. Data from odor pairs for which a mouse performed
721 fewer than 100 total trials were excluded from all analyses. Four sessions of go/no-go behavior were
722 excluded from analyses because of behavioral apparatus malfunctioning and three sessions were
723 excluded for improper laser parameters.

724

725 **FIGURES and FIGURE LEGENDS**

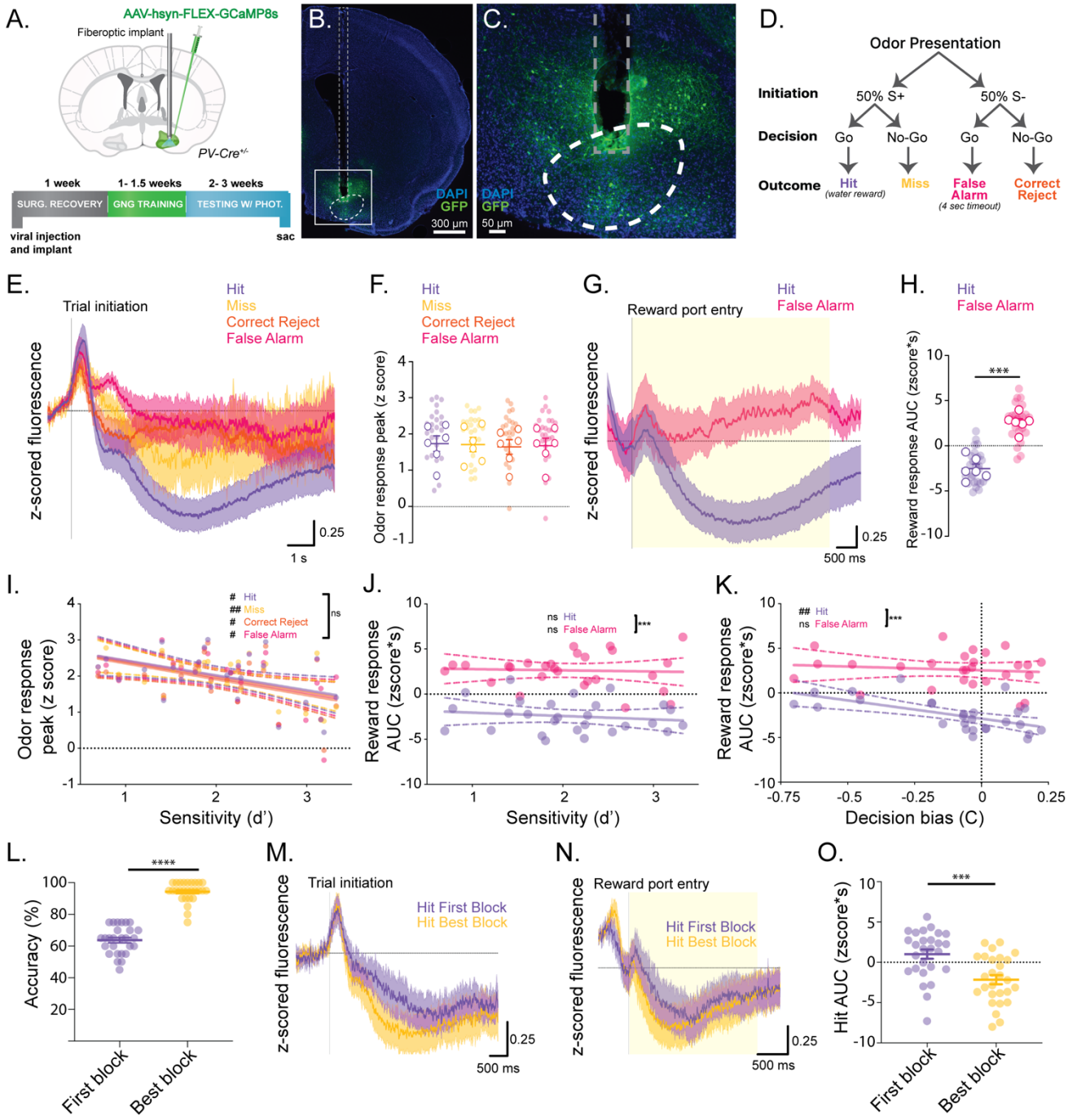

726

727 **Figure 1: BF PV neurons are excited by odor and suppressed by reward delivery.**

728 **A.** Schematic showing injection of Cre-dependent viral construct and fiberoptic implant in PV-Cre mice

729 (top). Highlighted regions of the BF include the horizontal limb of the diagonal band of broca (HDB), the

730 magnocellular preoptic nucleus (MCPO) and substantia innominata (SI). An experimental timeline

731 shows timing of surgery, behavioral training, and behavioral testing with fiber photometry imaging

732 (bottom). **B.** Example slice image showing the implant tract and expression of GCaMP. **C.** Viral
733 expression (green) and implant tip localization (dashed line) in the HDB. **D.** Schematic of olfactory-
734 cued go/no-go behavioral paradigm showing possible stimuli, decisions, and outcomes of individual
735 trials. **E.** Average z-scored GCaMP traces of the four trial types listed in D overlaid with 95%
736 confidence intervals (shaded regions). **F.** Peak signal amplitudes of the four trial types. Pastel circles
737 represent the peak odor response of each testing session. White circles represent the average peak
738 odor response of each animal. Line shows mean across animals. Error bars show SEM across animals.
739 **G.** Average z-scored GCaMP traces for Hit and False Alarm trials aligned to the time of reward port
740 entry with 95% confidence intervals overlaid (shaded regions). Yellow shaded area represents the time
741 over which the area under the curve (AUC) was quantified. **H.** Area under the curve (AUC) of Hit and
742 False Alarm traces across testing sessions. Transparent circles represent the AUC of each testing
743 session. White circles represent the average AUC of each animal. Lines show mean across animals
744 and error bars show SEM across animals. *** $p < 0.001$ paired t test across N = 6 animals. **I.**
745 Correlation of the peak odor responses with discrimination sensitivity (d') by trial type, across sessions.
746 Circles show values of odor response peaks for all trials of a given type within a session plotted against
747 the d' value for that session. Lines of best fit (solid lines) are shown for each trial type with 95%
748 confidence intervals (dashed lines). Hash tags indicate slopes of best fit lines that are significantly
749 different from zero. # $p < 0.05$, ## $p < 0.01$. Bracketed n.s. indicates that no best fit line slopes or
750 intercepts are significantly different across trial types. **J.** Correlation of the reward response area under
751 the curve (AUC) with discrimination sensitivity (d') by reward seeking trial type, across sessions. Circles
752 show values of odor response peaks for hit and false alarm trials within a session plotted against the d'
753 value for that session. Lines of best fit (solid lines) are shown for each trial type with 95% confidence
754 intervals (dashed lines). Slopes of each best fit line are not significantly different from zero (n.s.).
755 Bracketed asterisks indicate a significant difference between the y intercepts of the best fit lines (*** $p <$
756 0.001). **K.** Correlation of the reward response AUC with decision bias (C) by reward seeking trial type.
757 Circles show values of odor response peaks for hit and false alarm trials within a session plotted
758 against the C value for that session. Lines of best fit (solid lines) are shown for each trial type with 95%

759 confidence intervals (dashed lines). Hash tags indicate a best fit line slope significantly different from
760 zero (## $p < 0.01$). Bracketed asterisks indicate a significant difference between the y intercepts of the
761 best fit lines (*** $p < 0.001$). **L.** Accuracy (% correct trials) from first block of 20 trials in a session
762 (purple) compared to the block of 20 trials with highest accuracy in a session (yellow). Circles show
763 values for individual sessions with lines and error bars showing mean and SEM. **** $p < 0.0001$, paired
764 t test. **M.** Average traces (solid lines), aligned to the time of odor port entry (trial initiation), from hit
765 trials in first blocks (purple) and highest accuracy blocks (yellow) with 95% confidence intervals (shaded
766 regions). Horizontal line indicates baseline subtracted z score = 0. **N.** Average traces (solid lines),
767 aligned to the time of reward port entry, from hit trials in first blocks (purple) and highest accuracy
768 blocks (yellow) with 95% confidence intervals (shaded regions). Horizontal line indicates baseline
769 subtracted z score = 0. **O.** Quantification of the reward-related response (AUC) in hit trials from first
770 (purple) and best blocks (yellow). Circles show values for individual sessions with lines and error bars
771 showing mean and SEM. *** $p < 0.001$.

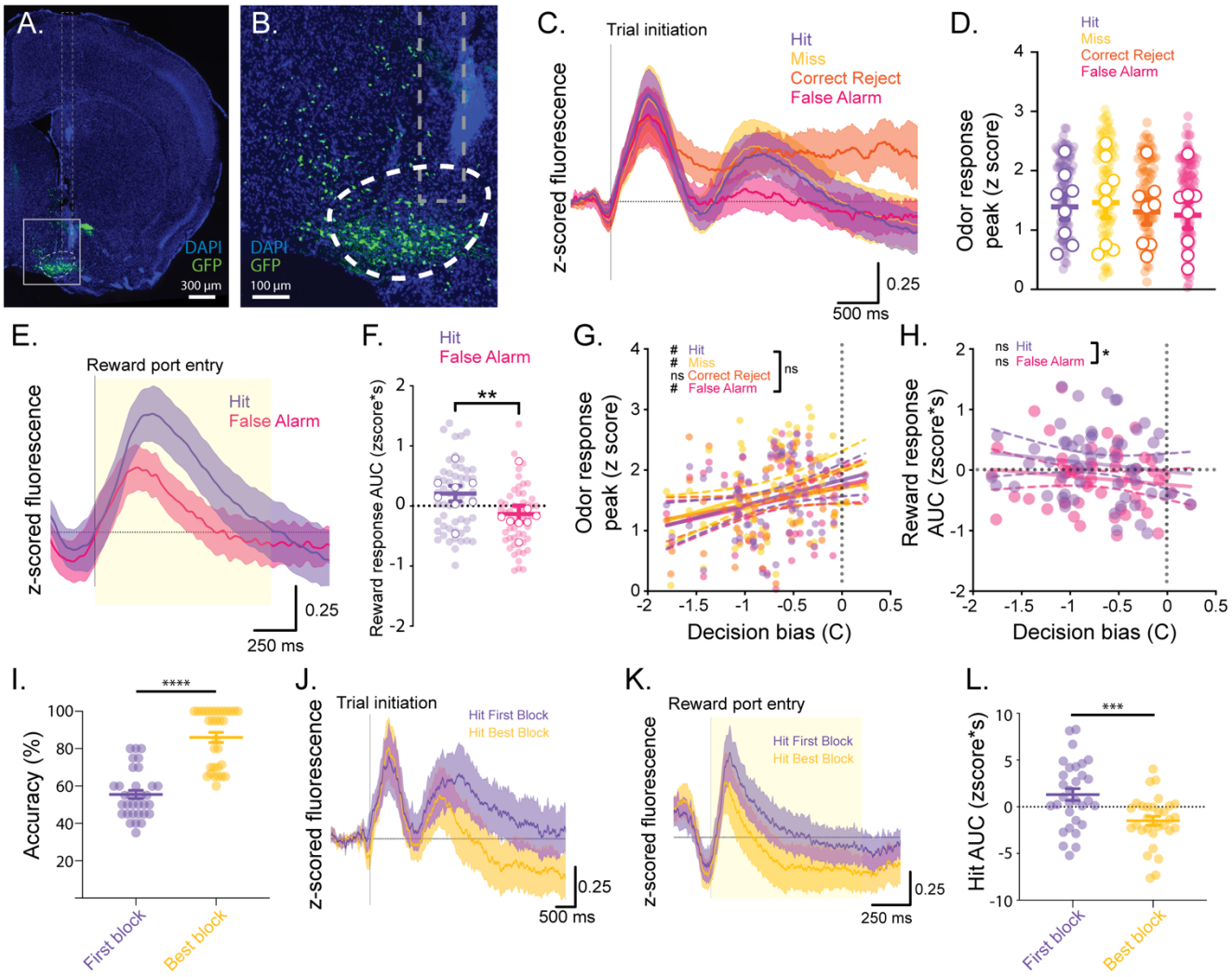

Figure 2: BF SST neurons are excited by odor and reward delivery.

A. Example slice image showing the implant tract and expression of GCaMP in the BF. **B.** Viral expression (green) and fiberoptic implant tip localization (dashed line) in the HDB. **C.** Average z-scored GCaMP traces of the four trial types across all sessions overlaid with 95% confidence intervals (shaded regions). **D.** Peak signal amplitudes of the four trial types. Light circles represent the peak odor response of each testing session. White circles represent the average peak odor response of each animal with mean and SEM of mouse averages. **E.** Average z-scored GCaMP traces for Hit and False Alarm trials, aligned to the time of reward port entry, with 95% confidence intervals (shaded regions). Yellow shaded area represents the time over which the area under the curve (AUC) of the reward response was calculated. **F.** Area under the curve (AUC) of Hit and False Alarm traces across testing

783 sessions. Transparent circles represent the AUC of each testing session. White circles represent the
784 average AUC of each animal with mean and SEM of mouse averages. ** $p < 0.01$ paired t test across N
785 = 8 animals. **G.** Correlation of peak odor response with decision bias (C) by trial types across sessions.
786 Circles show values of odor response peaks for all trials of a given type within a session plotted against
787 the C value for that session. Lines of best fit (solid lines) are shown for each trial type with 95%
788 confidence intervals (dashed lines). Hash tags indicate a best fit line slope significantly different from
789 zero (# $p < 0.05$). Bracketed n.s. indicates that no best fit line slopes are significantly different from
790 each other. **H.** Correlation of the reward response AUC with decision bias (C) by reward seeking trial
791 type. Circles show values of odor response peaks for hit and false alarm trials within a session plotted
792 against the C value for that session. Lines of best fit (solid lines) are shown for each trial type with 95%
793 confidence intervals (dashed lines). Slopes of each best fit line are not significantly different from zero
794 (n.s.). Bracketed asterisk indicates a significant difference between the y intercepts of the best fit lines
795 (* $p < 0.05$). **I.** Accuracy (% correct trials) from first block of 20 trials in a session (purple) compared to
796 the block of 20 trials with highest accuracy in a session (yellow). Circles show values for individual
797 sessions with lines and error bars showing mean and SEM. **** $p < 0.0001$, paired t test. **J.** Average
798 traces (solid lines), aligned to the time of odor port entry (trial initiation), from hit trials in first blocks
799 (purple) and highest accuracy blocks (yellow) with 95% confidence intervals (shaded regions).
800 Horizontal line indicates baseline subtracted z score = 0. **K.** Average traces (solid lines), aligned to the
801 time of reward port entry, from hit trials in first blocks (purple) and highest accuracy blocks (yellow) with
802 95% confidence intervals (shaded regions). Horizontal line indicates baseline subtracted z score = 0.
803 **L.** Quantification of the reward-related response (AUC) in hit trials from first (purple) and best blocks
804 (yellow). Circles show values for individual sessions with lines and error bars showing mean and SEM.
805 *** $p < 0.001$, paired t test.

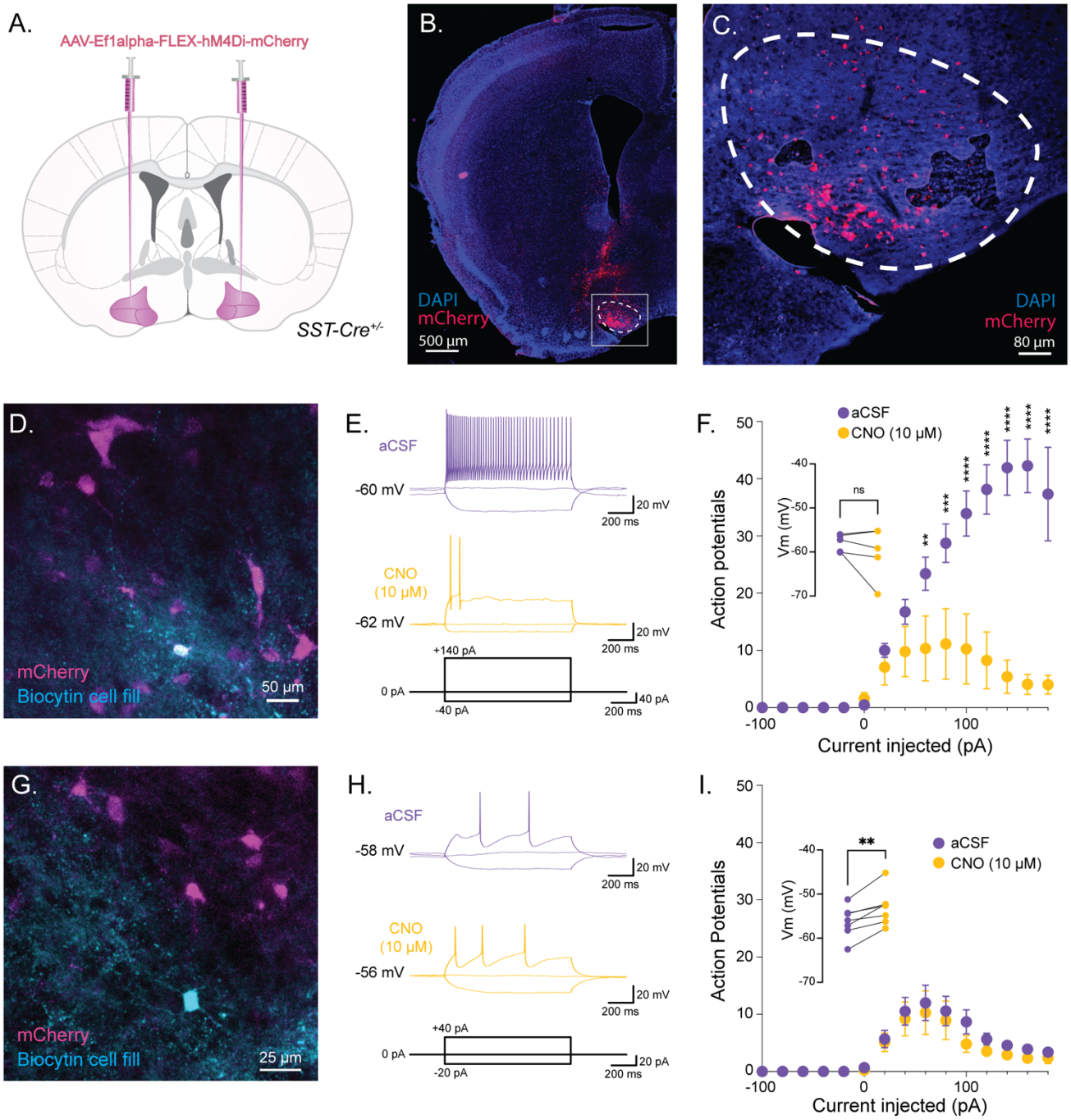

Figure 3: DREADD inhibition of SST neurons in slice does not impact firing of neighboring BF neurons. A. Schematic showing bilateral injection of Cre-dependent hM4Di viral construct into basal forebrain regions including the horizontal limb of the diagonal band of broca (HDB), magnocellular preoptic nucleus (MCPO), and substantia innominata (SI) of SST-Cre mice. **B.** Example of hM4Di-mCherry expression in BF with the HDB outlined. **C.** Inset from B showing hM4Di-mCherry expression in HDB. **D.** Example cell fill and hM4Di-mCherry expression from patched hM4Di-expressing

813 (mCherry+) SST neuron. **E.** Example responses to current injections in aCSF (top, purple) and after
814 CNO (10 μM) wash on (yellow middle). Bottom panel shows current injection schematic for example
815 traces. Traces are from cell shown in D. **F.** For hM4Di-expressing neurons: Quantification of action
816 potentials fired at each current injection in aCSF (purple) and after CNO wash on (yellow). n = 5 cells.
817 Circles show mean ± SEM. ** $p < 0.01$, *** $p < 0.001$, **** $p < 0.0001$, paired t test. Inset shows resting
818 membrane potential of each cell before (purple) and after (yellow) wash on of CNO. **G.** Example cell fill
819 and hM4Di-mCherry expression from patched neuron not expressing hM4Di. **H.** Example responses to
820 current injections in aCSF (top, purple) and after CNO (10 μM) wash on (yellow middle). Bottom panel
821 shows current injection schematic for example traces. Traces are from cell shown in G. **I.** For patched
822 neurons not expressing hM4Di: Quantification of action potentials fired at each current injection in
823 aCSF (purple) and after CNO wash on (yellow). Circles show mean ± SEM. Inset shows resting
824 membrane potential of each cell before (purple) and after (yellow) wash on of CNO. n = 7 cells. ** $p <$
825 0.01, paired t test.

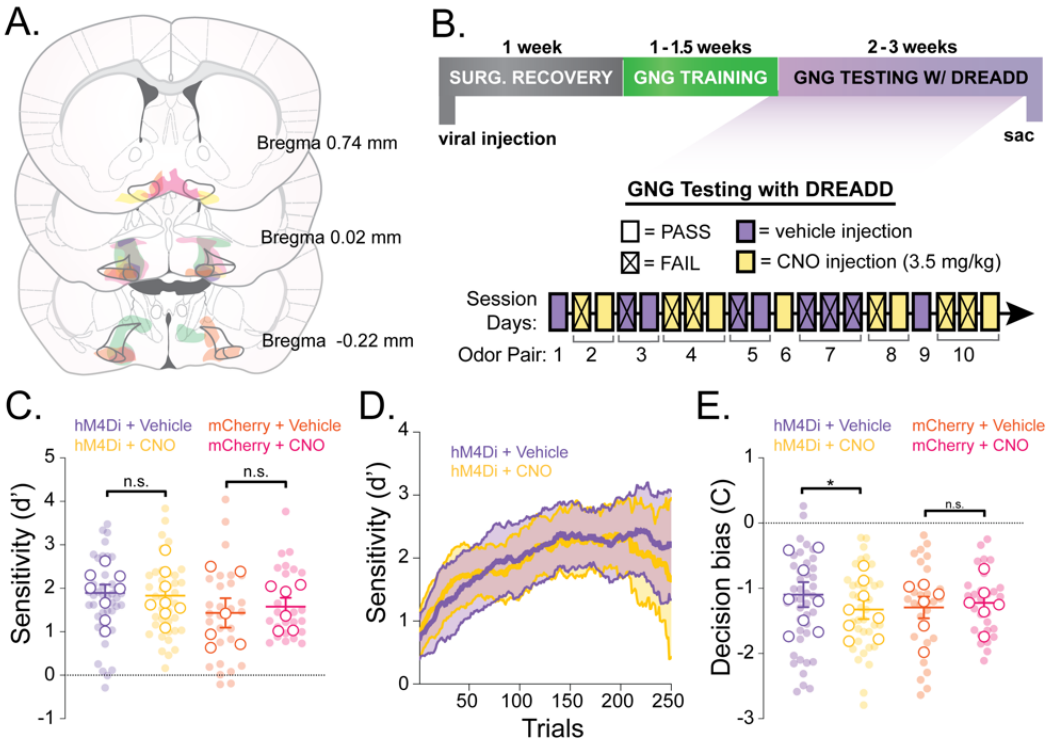

Figure 4: DREADD inhibition of SST neurons increases decision bias in the go/no-go task. **A.** Quantification of DREADD expression in each animal used for behavioral experiments. Shaded regions represent areas containing cells expressing hM4Di-mCherry across three coronal sections spanning AP from bregma -0.22 – 0.74 mm. Regions are color coded by animal (N = 8). **B.** Timeline of surgery, behavioral training, and behavioral testing with DREADD-mediated inhibition (top) and schematic of the CNO or vehicle injections during testing on different odor pairs (bottom). **C.** Average d' for individual sessions (transparent circles, n = 30-40) and mouse averages (white circles, N = 6-8) with mean and SEM of mouse averages. **D.** Performance of mice in the testing phase quantified as a rolling window of sensitivity (d') across trials. Averages of all CNO-treatment sessions are shown in yellow with 95% confidence intervals (shaded yellow). Averages of all vehicle-treatment sessions are shown in purple with 95% confidence intervals (shaded purple). **E.** Average criterion values for individual sessions (transparent circles) and mouse averages (white circles) with mean and SEM of mouse averages. * $p < 0.05$ paired t test between CNO and vehicle-treated sessions (n = 5 sessions per treatment per mouse) with hM4Di-expressing animals (N = 8 mice). n.s. $p > 0.05$ paired t test

842 between CNO and vehicle-treated sessions (n = 5 sessions per treatment per mouse) with mCherry-

843 expressing control animals (N = 6 mice).

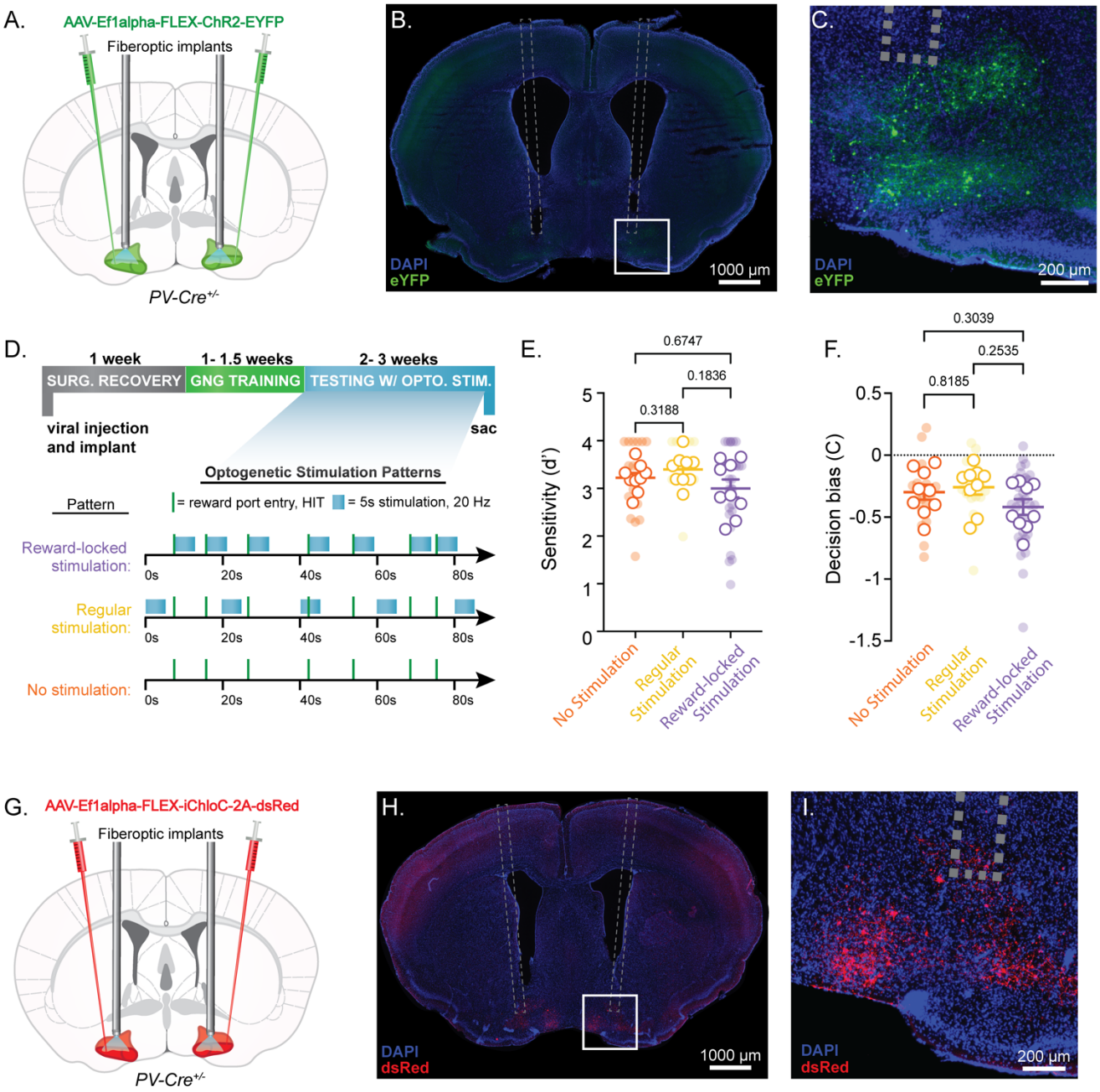
A.
AAV-Ef1alpha-FLEX-ChR2-EYFP
Fiberoptic implants
PV-Cre+/-
B.
DAPI
eYFP
1000 µm
C.
DAPI
eYFP
200 µm
D.
1 week
1- 1.5 weeks
2- 3 weeks
SURG. RECOVERY
GNG TRAINING
TESTING W/ OPTO. STIM.
viral injection and implant
sac
Optogenetic Stimulation Patterns
Pattern
= reward port entry, HIT
= 5s stimulation, 20 Hz
Reward-locked stimulation:
Regular stimulation:
No stimulation:
0s
20s
40s
60s
80s
E.
0.6747
0.1836
0.3188
Sensitivity (d')
No Stimulation
Regular Stimulation
Reward-locked Stimulation
F.
0.3039
0.2535
0.8185
Decision bias (C)
No Stimulation
Regular Stimulation
Reward-locked Stimulation
G.
AAV-Ef1alpha-FLEX-iChloC-2A-dsRed
Fiberoptic implants
PV-Cre+/-
H.
DAPI
dsRed
1000 µm
I.
DAPI
dsRed
200 µm
J.
1 week
1- 1.5 weeks
12 days
SURG. RECOVERY
GNG TRAINING
TESTING W/ OPTO. INHIB.
viral injection and implant
sac
Optogenetic Inihbition Patterns
Pattern
= odor port entry
= single 500 ms square pulse
Stimulation on all trials (All):
Stimulation on random trials (Random):
Control stimulation:
0s
20s
40s
60s
80s
K.
*
ns
*
Sensitivity (d')
Control
Random trials
All trials
L.
0.9985
0.5004
0.2665
Decision bias (C)
Control
Random trials
All trials

844

845 **Figure 5: Optogenetic manipulations of PV neurons during odor cue and reward.**

846 **A.** Schematic showing bilateral injection of Cre-dependent ChR2 viral construct and fiberoptic implant in
847 PV-Cre mice. Green-highlighted regions of the BF include the horizontal limb of the diagonal band of
848 broca (HDB), the magnocellular preoptic nucleus (MCPO) and substantia innominata (SI). **B.** Example
849 slice image showing the implant tract, expression of ChR2-eYFP (green), and DAPI (blue). **C.** Viral
850 expression (green) and implant tip localization (dashed line) in the HDB. **D.** Timeline of surgery,
851 behavioral training, and behavioral testing with optogenetic stimulation (top) and schematic outlining the
852 different optogenetic stimulation experimental conditions (bottom). **E.** Summary d' for individual
853 sessions, calculated as the maximum d' from a 40-trial rolling window over the course of a session (see
854 methods) (transparent circles, n = 19 no stimulation sessions, 18 regular stimulation sessions, and 30
855 reward-locked stimulation sessions). Mouse averages of summary d' values are shown as white circles
856 with mean and SEM (N = 9 mice, p values from RM one-way ANOVA with multiple comparisons using
857 Tukey correction). **F.** Average criterion values for individual sessions (transparent circles) and mouse
858 averages (white circles) with mean and SEM of mouse averages. **G.** Schematic showing bilateral
859 injection of Cre-dependent iChloC viral construct and fiberoptic implant in PV-Cre mice. Red-highlighted
860 regions of the BF include the horizontal limb of the diagonal band of broca (HDB), the magnocellular
861 preoptic nucleus (MCPO) and substantia innominata (SI). **H.** Example slice image showing the implant
862 tract and expression of iChloC-dsRed. **I.** Viral expression and implant tip localization in the HDB. **J.**
863 Timeline of surgery, behavioral training, and behavioral testing with optogenetic inhibition (top) and
864 schematic outlining the different optogenetic inhibition experimental conditions (bottom). **K.** Summary
865 d' for individual sessions, calculated as the maximum d' from a 40-trial rolling window over the course
866 of a session (transparent circles, n = 8 control sessions, 14 random trial stimulation sessions, and 10 all
867 trial stimulation sessions). Mouse averages of summary d' values are shown as white circles with mean
868 and SEM (N = 5 mice, Control vs. All p = 0.029, Random vs All p = 0.041, *p < 0.05, RM one-way
869 ANOVA with multiple comparisons using Tukey correction). **L.** Average criterion values for individual
870 sessions (transparent circles) and mouse averages (white circles) with mean and SEM of mouse
871 averages.

872 **REFERENCES**

873 Agostinelli LJ, Geerling JC, Scammell TE (2019) Basal forebrain subcortical projections. Brain Struct
874 Funct 224:1097–1117.

875 Anaclet C, de Luca R, Venner A, Malyshevskaya O, Lazarus M, Arrigoni E, Fuller PM (2018) Genetic
876 activation, inactivation, and deletion reveal a limited and nuanced role for somatostatin-containing
877 basal forebrain neurons in behavioral state control. Journal of Neuroscience 38:5168–5181.

878 Anaclet C, Pedersen NP, Ferrari LL, Venner A, Bass CE, Arrigoni E, Fuller PM (2015) Basal forebrain
879 control of wakefulness and cortical rhythms. Nat Commun 6:8744.

880 Ballinger EC, Ananth M, Talmage DA, Role LW (2016) Basal forebrain cholinergic circuits and signaling
881 in cognition and cognitive decline. Neuron 91:1199–1218.

882 Bendahmane M, Ogg MC, Ennis M, Fletcher ML (2016) Increased olfactory bulb acetylcholine bi-
883 directionally modulates glomerular odor sensitivity. Sci Rep 6:1–13.

884 Bigl V, Woolf NJ, Butcher LL (1982) Cholinergic projections from the basal forebrain to frontal, parietal,
885 temporal, occipital, and cingulate cortices: a combined fluorescent tracer and acetylcholinesterase
886 analysis. Brain Res Bull 8:727–749.

887 Böhm E, Brunert D, Rothermel M (2020) Input dependent modulation of olfactory bulb activity by HDB
888 GABAergic projections. Sci Rep 10:1–15.

889 Castillo PE, Carleton A, Vincent J-D, Lledo P-M (1999) Multiple and opposing roles of cholinergic
890 transmission in the main olfactory bulb. Journal of Neuroscience 19:9180–9191.

891 Chaudhury D, Escanilla O, Linster C (2009) Bulbar acetylcholine enhances neural and perceptual odor
892 discrimination. Journal of Neuroscience 29:52–60.

893 Chaves-Coira I, Barros-Zulaica N, Rodrigo-Angulo M, Núñez Á (2016) Modulation of specific sensory
894 cortical areas by segregated basal forebrain cholinergic neurons demonstrated by neuronal tracing
895 and optogenetic stimulation in mice. Front Neural Circuits 10:28.

896 de Saint Jan D (2022) Target-specific control of olfactory bulb periglomerular cells by GABAergic and
897 cholinergic basal forebrain inputs. Elife 11:e71965.

898 Devore S, Pender-Morris N, Dean O, Smith D, Linster C (2015) Basal forebrain dynamics during
899 nonassociative and associative olfactory learning. J Neurophysiol 115:423–433.
900 Do JP, Xu M, Lee S-H, Chang W-C, Zhang S, Chung S, Yung TJ, Fan JL, Miyamichi K, Luo L (2016)
901 Cell type-specific long-range connections of basal forebrain circuit. Elife 5:e13214.
902 Elaagouby A, Ravel N, Gervais R (1991) Cholinergic modulation of excitability in the rat olfactory bulb:
903 effect of local application of cholinergic agents on evoked field potentials. Neuroscience 45:653–
904 662.
905 Fisher RS, Buchwald NA, Hull CD, Levine MS (1988) GABAergic basal forebrain neurons project to the
906 neocortex: the localization of glutamic acid decarboxylase and choline acetyltransferase in feline
907 corticopetal neurons. Journal of Comparative Neurology 272:489–502.
908 Gielow MR, Zaborszky L (2017) The input-output relationship of the cholinergic basal forebrain. Cell
909 Rep 18:1817–1830.
910 Goard M, Dan Y (2009) Basal forebrain activation enhances cortical coding of natural scenes. Nat
911 Neurosci 12:1444–1449.
912 Gracia-Llanes FJ, Crespo C, Blasco-Ibáñez JM, Nacher J, Varea E, Rovira-Esteban L, Martínez-
913 Guijarro FJ (2010) GABAergic basal forebrain afferents innervate selectively GABAergic targets in
914 the main olfactory bulb. Neuroscience 170:913–922.
915 Gritton HJ, Howe WM, Mallory CS, Hetrick VL, Berke JD, Sarter M (2016) Cortical cholinergic signaling
916 controls the detection of cues. Proceedings of the National Academy of Sciences 113:E1089–
917 E1097.
918 Grothe M, Zaborszky L, Atienza M, Gil-Neciga E, Rodriguez-Romero R, Teipel SJ, Amunts K, Suarez-
919 Gonzalez A, Cantero JL (2010) Reduction of basal forebrain cholinergic system parallels cognitive
920 impairment in patients at high risk of developing Alzheimer's disease. Cerebral Cortex 20:1685–
921 1695.
922 Hangya B, Ranade SP, Lorenc M, Kepecs A (2015) Central cholinergic neurons are rapidly recruited by
923 reinforcement feedback. Cell 162:1155–1168.

924 Hanson E, Brandel-Ankrapp KL, Arenkiel BR (2021) Dynamic cholinergic tone in the basal forebrain
925 reflects reward-seeking and reinforcement during olfactory behavior. Front Cell Neurosci
926 15:635837.
927 Hanson E, Swanson J, Arenkiel BR (2020) GABAergic Input From the Basal Forebrain Promotes the
928 Survival of Adult-Born Neurons in the Mouse Olfactory Bulb. Front Neural Circuits 14.
929 Harrison TC, Pinto L, Brock JR, Dan Y (2016) Calcium imaging of basal forebrain activity during innate
930 and learned behaviors. Front Neural Circuits 10:36.
931 Hassani OK, Lee MG, Henny P, Jones BE (2009) Discharge profiles of identified GABAergic in
932 comparison to cholinergic and putative glutamatergic basal forebrain neurons across the sleep–
933 wake cycle. Journal of Neuroscience 29:11828–11840.
934 Hasselmo ME (1999) Neuromodulation: acetylcholine and memory consolidation. Trends Cogn Sci
935 3:351–359.
936 Hasselmo ME, McGaughy J (2004) High acetylcholine levels set circuit dynamics for attention and
937 encoding and low acetylcholine levels set dynamics for consolidation. Prog Brain Res 145:207–
938 231.
939 Herman AM, Ortiz-Guzman J, Kochukov M, Herman I, Quast KB, Patel JM, Tepe B, Carlson JC, Ung K,
940 Selever J (2016) A cholinergic basal forebrain feeding circuit modulates appetite suppression.
941 Nature 538:253–256.
942 Herrero JL, Roberts MJ, Delicato LS, Gieselmann MA, Dayan P, Thiele A (2008) Acetylcholine
943 contributes through muscarinic receptors to attentional modulation in V1. Nature 454:1110–1114.
944 Kim T, Thankachan S, McKenna JT, McNally JM, Yang C, Choi JH, Chen L, Kocsis B, Deisseroth K,
945 Strecker RE, Basheer R, Brown RE, McCarley RW (2015) Cortically projecting basal forebrain
946 parvalbumin neurons regulate cortical gamma band oscillations. Proceedings of the National
947 Academy of Sciences 112:201413625.
948 Lau B, Salzman CD (2008) Noncholinergic neurons in the basal forebrain: often neglected but
949 motivationally salient. Neuron 59:6–8.

950 Ledbetter NM, Chen CD, Monosov IE (2016) Multiple mechanisms for processing reward uncertainty in
951 the primate basal forebrain. Journal of Neuroscience 36:7852–7864.
952 Levin ED, Simon BB (1998) Nicotinic acetylcholine involvement in cognitive function in animals.
953 Psychopharmacology (Berl) 138:217–230.
954 Lin S-C, Nicolelis MAL (2008) Neuronal ensemble bursting in the basal forebrain encodes salience
955 irrespective of valence. Neuron 59:138–149.
956 Ma M, Luo M (2012) Optogenetic Activation of Basal Forebrain Cholinergic Neurons Modulates
957 Neuronal Excitability and Sensory Responses in the Main Olfactory Bulb. The Journal of
958 Neuroscience 32:10105–10116.
959 Mandairon N, Ferretti CJ, Stack CM, Rubin DB, Cleland TA, Linster C (2006) Cholinergic modulation in
960 the olfactory bulb influences spontaneous olfactory discrimination in adult rats. European Journal
961 of Neuroscience 24:3234–3244.
962 Markram H, Segal M (1990) Long-lasting facilitation of excitatory postsynaptic potentials in the rat
963 hippocampus by acetylcholine. J Physiol 427:381–393.
964 McDonald AJ, Muller JF, Mascagni F (2011) Postsynaptic targets of GABAergic basal forebrain
965 projections to the basolateral amygdala. Neuroscience 183:144–159.
966 Muir JL, Page KJ, Sirinathsinghji DJS, Robbins TW, Everitt BJ (1993) Excitotoxic lesions of basal
967 forebrain cholinergic neurons: effects on learning, memory and attention. Behavioural brain
968 research 57:123–131.
969 Nunez-Parra A, Maurer RK, Krahe K, Smith RS, Araneda RC (2013) Disruption of centrifugal inhibition
970 to olfactory bulb granule cells impairs olfactory discrimination. Proceedings of the National
971 Academy of Sciences 110:14777–14782.
972 Nunez-Parra A, Rio C-D, Christian A, Huntsman MM, Restrepo D (2020) The basal forebrain modulates
973 neuronal response in an active olfactory discrimination task. Front Cell Neurosci 14:141.
974 Ogg MC, Ross JM, Bendahmane M, Fletcher ML (2018) Olfactory bulb acetylcholine release
975 dishabituates odor responses and reinstates odor investigation. Nat Commun 9:1–11.

976 Parikh V, Kozak R, Martinez V, Sarter M (2007) Prefrontal acetylcholine release controls cue detection
977 on multiple timescales. Neuron 56:141–154.
978 Parrao T, Chana P, Venegas P, Behrens MI, Aylwin ML (2012) Olfactory deficits and cognitive
979 dysfunction in Parkinson's disease. Neurodegener Dis 10:179–182.
980 Patel JM, Swanson J, Ung K, Herman A, Hanson E, Ortiz-Guzman J, Selever J, Tong Q, Arenkiel BR
981 (2019) Sensory perception drives food avoidance through excitatory basal forebrain circuits. Elife
982 8.
983 Phillis JW (1968) Acetylcholine release from the cerebral cortex: its role in cortical arousal. Brain Res
984 7:378–389.
985 Pinto L, Goard MJ, Estandian D, Xu M, Kwan AC, Lee S-H, Harrison TC, Feng G, Dan Y (2013) Fast
986 modulation of visual perception by basal forebrain cholinergic neurons. Nat Neurosci 16:1857–
987 1863.
988 Rothermel M, Carey RM, Puche A, Shipley MT, Wachowiak M (2014) Cholinergic inputs from Basal
989 forebrain add an excitatory bias to odor coding in the olfactory bulb. Journal of Neuroscience
990 34:4654–4664.
991 Rothermel M, Wachowiak M (2014) Functional imaging of cortical feedback projections to the olfactory
992 bulb. Front Neural Circuits 8:73.
993 Ruivo LMT-G, Baker KL, Conway MW, Kinsley PJ, Gilmour G, Phillips KG, Isaac JTR, Lowry JP, Mellor
994 JR (2017) Coordinated acetylcholine release in prefrontal cortex and hippocampus is associated
995 with arousal and reward on distinct timescales. Cell Rep 18:905–917.
996 Sanz Diez A, Najac M, De Saint Jan D (2019) Basal forebrain GABAergic innervation of olfactory bulb
997 periglomerular interneurons. J Physiol 597:2547–2563.
998 Sarter M, Bruno JP (1997) Cognitive functions of cortical acetylcholine: toward a unifying hypothesis.
999 Brain Res Rev 23:28–46.
1000 Sarter M, Bruno JP (1999) Cortical cholinergic inputs mediating arousal, attentional processing and
1001 dreaming: differential afferent regulation of the basal forebrain by telencephalic and brainstem
1002 afferents. Neuroscience 95:933–952.

1003 Sarter M, Bruno JP, Turchi J (1999) Basal forebrain afferent projections modulating cortical
1004 acetylcholine, attention, and implications for neuropsychiatric disorders. Ann N Y Acad Sci
1005 877:368–382.
1006 Sarter M, Givens B, Bruno JP (2001) The cognitive neuroscience of sustained attention: where top-
1007 down meets bottom-up. Brain Res Rev 35:146–160.
1008 Semba K (1991) The cholinergic basal forebrain: a critical role in cortical arousal. The basal
1009 forebrain:197–218.
1010 Stanislaw H, Todorov N (1999) Calculation of signal detection theory measures. Behavior research
1011 methods, instruments, & computers 31:137–149.
1012 Szymusiak R (1995) Magnocellular nuclei of the basal forebrain: substrates of sleep and arousal
1013 regulation. Sleep 18:478–500.
1014 Szymusiak R, Alam N, McGinty D (2000) Discharge patterns of neurons in cholinergic regions of the
1015 basal forebrain during waking and sleep. Behavioural brain research 115:171–182.
1016 Tashakori-Sabzevar F, Ward RD (2018) Basal forebrain mediates motivational recruitment of attention
1017 by reward-associated cues. Front Neurosci 12:786.
1018 Tingley D, Alexander AS, Quinn LK, Chiba AA, Nitz DA (2015) Cell assemblies of the basal forebrain.
1019 Journal of Neuroscience 35:2992–3000.
1020 Tsuno Y, Kashiwadani H, Mori K (2008) Behavioral state regulation of dendrodendritic synaptic
1021 inhibition in the olfactory bulb. Journal of Neuroscience 28:9227–9238.
1022 Villar PS, Hu R, Araneda RC (2020) Long-range GABAergic inhibition modulates spatiotemporal
1023 dynamics of the output neurons in the olfactory bulb. bioRxiv.
1024 Woolf NJ, Hernit MC, Butcher LL (1986) Cholinergic and non-cholinergic projections from the rat basal
1025 forebrain revealed by combined choline acetyltransferase and Phaseolus vulgaris leucoagglutinin
1026 immunohistochemistry. Neurosci Lett 66:281–286.
1027 Xu M, Chung S, Zhang S, Zhong P, Ma C, Chang W-C, Weissbourd B, Sakai N, Luo L, Nishino S
1028 (2015) Basal forebrain circuit for sleep-wake control. Nat Neurosci 18:1641–1647.

1029 Zaborszky L, Carlsen J, Brashear HR, Heimer L (1986) Cholinergic and GABAergic afferents to the
1030 olfactory bulb in the rat with special emphasis on the projection neurons in the nucleus of the
1031 horizontal limb of the diagonal band. Journal of Comparative Neurology 243:488–509.
1032 Zaborszky L, Duque A (2000a) Local synaptic connections of basal forebrain neurons. Behavioural
1033 brain research 115:143–158.
1034 Zaborszky L, Duque A (2000b) Local synaptic connections of basal forebrain neurons. Behavioural
1035 brain research 115:143–158.
1036 Zant JC, Kim T, Prokai L, Szarka S, McNally J, McKenna JT, Shukla C, Yang C, Kalinchuk A v,
1037 McCarley RW (2016) Cholinergic neurons in the basal forebrain promote wakefulness by actions
1038 on neighboring non-cholinergic neurons: an opto-dialysis study. Journal of Neuroscience 36:2057–
1039 2067.
1040 Zhang K, Chen CD, Monosov IE (2019) Novelty, salience, and surprise timing are signaled by neurons
1041 in the basal forebrain. Current Biology 29:134–142.
1042 Zheng Y, Feng S, Zhu X, Jiang W, Wen P, Ye F, Rao X, Jin S, He X, Xu F (2018) Different subgroups
1043 of cholinergic neurons in the basal forebrain are distinctly innervated by the olfactory regions and
1044 activated differentially in olfactory memory retrieval. Front Neural Circuits 12:99.
1045 Zheng Y, Tao S, Liu Y, Liu J, Sun L, Zheng Y, Tian Y, Su P, Zhu X, Xu F (2022) Basal Forebrain-Dorsal
1046 Hippocampus Cholinergic Circuit Regulates Olfactory Associative Learning. Int J Mol Sci 23:8472.
1047